OXFORD

Journal of Petrology, 2023, **64**, 1–32
https://doi.org/10.1093/petrology/egad073
Advance access publication date 3 October 2023
Original Manuscript

Petrology and Geochemistry of Adak Island Plutonic Xenoliths: Implications for Primitive Magma Generation and Crustal Differentiation in the Aleutian Island Arc

Emma S. Sosa [1,*], Claire E. Bucholz[1], Mattison H. Barickman[2], Jill A. VanTongeren[3], Jacob B. Setera [4,†], Suzanne Mahlburg Kay[5] and Robert W. Kay[5]

[1]Division of Geological and Planetary Sciences, California Institute of Technology, Pasadena, CA 91125
[2]HDR Inc, 369 Inverness Pkwy, Ste 325, Englewood, CO 80112
[3]Department of Earth and Ocean Sciences, Tufts University, Medford, MA 02155
[4]Department of Earth and Planetary Sciences, Rutgers University, Piscataway, NJ, 08854
[5]Department of Earth and Atmospheric Sciences, Cornell University, Ithaca, NY 14850

*Corresponding author. Email: esosa@caltech.edu
†Present address: Center for the Advancement of Space Safety and Mission Assurance Research (CASSMAR), University of Texas at El Paso-Jacobs JETS II Contract, NASA Johnson Space Center, Houston, TX 77058

Abstract

Deep crustal cumulates in arcs offer a window into the chemistry and crystallization conditions (P–T–H_2O–fO_2) of primitive basalts in the upper mantle and lower crust and can be studied in ancient exhumed terranes or in xenoliths erupted in young arc lavas. Here, we expand on previous studies and thoroughly characterize the extensive xenolith suites erupted from the Mt. Moffett and Mt. Adagdak volcanic centers (Adak Island, Central Aleutians), which range from primitive ultramafic cumulates to more evolved amphibole gabbros and hornblendites. We present detailed petrography as well as *in situ* trace and major element mineral chemistry. We use these data to calculate pressure, temperature, and fO_2 estimates for the xenoliths, and compare these findings to experimental results to understand the crystallization sequence and P–T–H_2O–fO_2 under which the cumulates formed. The Moffett crystallization sequence is defined by early amphibole fractionation and an abrupt shift in oxide compositions from chromite to magnetite, while the Adagdak suite is characterized by simultaneous saturation of amphibole+plagioclase and oxide compositions that become increasingly aluminous before magnetite saturation. Olivine–spinel oxybarometry of the Adagdak xenoliths indicates that they are oxidized relative to mid-ocean ridge basalt (MORB:FMQ +0.1 to +2.1). Highly fractionated REE and elevated Sr/Y ratios are observed in clinopyroxene from the most primitive cumulates, consistent with a contribution from a basaltic eclogite melt. This basaltic eclogite melt is hypothesized to come from partial melting of the slab or through melting of basalt introduced into the subarc mantle through forearc subduction erosion. These signatures are greatly diminished in the more evolved lithologies, which can be explained through fractionation of plagioclase and amphibole. Our findings support the presence of a complex magmatic plumbing system beneath Adak, with Mt. Moffett and Mt. Adagdak volcanic centers tapping compositionally distinct sources. More broadly, our results are consistent with studies suggesting that low-degree basaltic eclogite melts through slab melting or forearc subduction erosion contribute to arc magmas in the Aleutians, although the associated geochemical signatures are easily obscured by differentiation in the crust.

Key words: Adak Island; Central Aleutians; cumulates; island arc; xenoliths

INTRODUCTION

Partial melting of subducted oceanic crust has long been evoked in models pertaining to the origin of convergent-margin magmas (Ringwood & Green, 1966; Green & Ringwood, 1968; Kay, 1978, 1980; Defant & Drummond, 1990; Drummond & Defant, 1990). Experimental studies show that low-degree partial melting of oceanic basalts metamorphosed to eclogite facies produces magmas with fractionated rare earth element (REE) patterns (La/Yb 40–55), depletions in high field strength elements (HFSE, Nb/La 0.1–0.4), and high Sr concentrations (800–1500 μg/g) (Rapp *et al.*, 1999). These signatures are attributed to the presence of garnet and rutile and lack of plagioclase in the eclogitic protoliths (Rapp *et al.*, 1999; Sisson & Kelemen, 2018). However, numerical modeling studies in the 1990s questioned both the capacity of dehydrated ocean crust to melt under conditions relevant to the subduction channel (Davies & Stevenson, 1992; Peacock *et al.*, 1994; Yasuda *et al.*, 1994) and the effectiveness by which these melts could segregate from their residues (Vigneresse *et al.*, 1996).

Thermal modeling (van Keken *et al.*, 2002; Peacock *et al.*, 2005; Wada & Wang, 2009; Syracuse *et al.*, 2010; Peacock, 2020), however, suggests that slab-top geotherms may intersect the wet-solidus of basaltic eclogite (Supplemental Data Figure S1, Schmidt & Poli, 1998; Poli & Schmidt, 2002; Sisson & Kelemen, 2018). Furthermore, refined models of partial melts of eclogite reacting with mantle wedge peridotite can reproduce major and trace element characteristics of primitive arc magmas (e.g. Sisson & Kelemen, 2018). Recently, Turner & Langmuir (2022a, 2022b) supported a general model, accounting for global variations in arc magma geochemistry, in which subducted altered oceanic crust (AOC) and sediment ubiquitously melt and are mixed into a mantle wedge

Received: January 18, 2023. **Revised:** September 21, 2023. **Accepted:** September 23, 2023

that varies in composition from a depleted MORB source to an enriched mantle. In this model, variable degrees of melting of these hybridized mantle compositions account for geochemical variations across and within arc systems. Slab melt signatures may also be introduced into the mantle wedge through subduction erosion, a process in which crustal material from the upper plate is eroded and brought to the subarc mantle via the subduction channel. Metamorphism and partial melting of this material with increased pressure and temperature may also create 'slab-melt' signatures (Bourgois *et al.*, 1996; Goss & Kay, 2006; Jicha & Kay, 2018; Kay *et al.*, 2019).

The Aleutians have been extensively studied to understand the contribution of subducted slab melts and forearc subduction erosion to the geochemistry of lavas and plutonic rocks (Kay, 1978, 1980; Kay & Kay, 1994; Yogodzinski *et al.*, 1994; Yogodzinski & Kelemen, 1998; Kelemen *et al.*, 2003a; Yogodzinski & Kelemen, 2007; Yogodzinski *et al.*, 2017; Jicha & Kay, 2018; Kay *et al.*, 2019; Bezard *et al.*, 2021). Slab melts in the source region of magmas have been inferred both from the presence of primitive high magnesium andesites (i.e. adakites; Kay, 1978; Yogodzinski *et al.*, 1994; Yogodzinski & Kelemen, 1998; Kelemen *et al.*, 2003a) and from studies of primitive lower crustal cumulates with adakite-like trace element signatures (e.g. fractionated REE patterns, high Sr/Y; Yogodzinski & Kelemen, 2007). Although primitive adakites rarely erupt in the central arc around Adak and are not observed in the eastern arc, some authors have suggested that some degree of slab melting may be common across the entire arc (Kelemen *et al.*, 2003a; Yogodzinski *et al.*, 2015).

Lower crustal, ultramafic cumulate xenoliths from Mt. Moffett on Adak Island have been used to support the inference that slab melting has occurred in the central Aleutians by Yogodzinski & Kelemen (2007), who analyzed trace elements in clinopyroxene from two olivine+amphibole clinopyroxenite xenoliths and found that they had elevated Sr/Y (5.1–47.2) and La/Yb (1.2–2.6) ratios which were positively correlated with Mg#. They proposed the correlation between high Sr/Y, La/Yb, and Mg# suggested that the slab melt component was strongest in the parental melts to the most primitive xenoliths, but was then diluted by reactions within the mantle or mixing with diverse melts within the crust or upper mantle (similar to inferences from previous studies: Kay, 1978, Yogodzinski *et al.*, 1994; Kelemen *et al.*, 2003a). Others have used the plutonic record on Adak Island to suggest that slab melting signatures on Adak may reflect subduction erosion and partial melting of mafic forearc material, at least locally (Jicha & Kay, 2018; Kay *et al.*, 2019). Pairing pluton Ar/Ar ages with trace element chemistry, Jicha & Kay (2018) and Kay *et al.* (2019) showed that arc migration, a feature associated with periods of increased forearc subduction erosion (Stern, 1991; von Huene & Scholl, 1991; Kay & Kay, 1994; Kay *et al.*, 2005; Goss *et al.*, 2013), coincided with the emplacement of the plutonic units with the strongest adakite-like signatures. In summary, while it is generally agreed that the geochemical characteristics of high-Mg andesites and xenoliths found on Adak necessitate mixing/reaction with partial melts of a basaltic eclogite, different possible sources for this end-member component have been proposed in the literature.

Here, we further explore the origin and characteristics of the parental magmas to xenoliths found in lava flows from Mt. Moffett and Adagdak volcano on Adak Island and their chemical evolution during differentiation. Although the mineralogy and chemistry of the xenoliths have been studied in the past (Conrad & Kay, 1984; Debari *et al.*, 1987), we characterize a larger suite of Adak xenoliths than previously described, including a previously undocumented mantle xenolith, in terms of major (Moffett: n = 12, Adagdak: n = 34) and trace element (Adagdak: n = 15, Moffett: n = 6) mineral chemistry. With these data, we calculate crystallization conditions (P, T, H_2O, fO_2) and parental melt trace element compositions. We then model the origin of the parental melts through basaltic eclogite melt-peridotite reactions and discuss the effect of fractional crystallization on the geochemical signatures of these hybridized melts. As the processes of slab melting and forearc subduction erosion should create melts with the same major and trace element characteristics, and the data we present here are not suitable to distinguish between the two processes, we use the term basaltic eclogite melt to refer to situations in which the source of this endmember component is ambiguous and could have resulted from either (or both) of these processes.

GEOLOGIC SETTING AND PREVIOUS WORK

Adak Island

Adak Island is part of the Andreanof crustal block in the central Aleutian arc (Fig. 1a) (Geist *et al.*, 1988). The island has two young stratovolcanoes, Mount Moffett and Mount Adagdak, which are located in the northern part of the island ~5 km apart (Fig. 1b). Mount Moffett has erupted in the Holocene (Jicha & Kay, 2018), and Mount Adagdak was active during the Pleistocene (Baten Soyini, 2002). Lavas from Adagdak and Moffett range from high-Mg basalts to dacites (Coats, 1956). Plutonic rocks exposed on Adak Island include the ~38 Ma Finger Bay pluton in the north-central part of the island, the ~35–31 Ma Hidden Bay pluton to the south, and the ~14 Ma Kagalaska pluton on the far eastern terminus of the island (Kay *et al.*, 1990, 2019; Kay & Kay, 1994; Jicha *et al.*, 2006). The Finger Bay pluton comprises amphibole-poor tholeiitic gabbros with subordinate quartz monzonites, and (quartz) monzodiorites (Kay *et al.*, 1983), whereas the larger Hidden Bay and Kagalaska plutons consist of amphibole-rich calc-alkaline gabbros, diorites, granodiorites, and minor leucogranodiorite (Fraser & Snyder, 1959; Citron *et al.*, 1980; Kay *et al.*, 2019).

Adak Island xenoliths—geologic context and previous work

The Moffett xenolith suite was collected from a ~100 m thick lava flow on the north/northeastern slopes of Mount Moffett (Coats, 1956; Conrad *et al.*, 1983; Conrad & Kay, 1984). A bulk-rock analysis of the xenolith-bearing flow is provided in the appendix of Kay & Kay (1994) (sample MFHOS). The Mount Adagdak xenoliths are exposed in an olivine-phyric, high-MgO (11.8 wt %) Holocene basaltic flow on the western slopes of the volcano (Debari *et al.*, 1987; Fig. 1b). Xenoliths from the Moffett and Adagdak flows have been the subject of thorough petrographic and geochemical studies (Conrad *et al.*, 1983; Conrad & Kay, 1984; Debari *et al.*, 1987) with additional trace element studies from two Moffett xenoliths documented by Yogodzinski & Kelemen (2007). We briefly describe these previous studies and their findings to establish a baseline for our further investigation of these xenoliths. The petrography and mineral chemistry of Adak xenoliths provided by these earlier works is summarized in Table 1.

Mount Adagdak

Debari *et al.* (1987) described the petrography and major element mineral chemistry of 10 cumulate xenoliths from Mount Adagdak, including dunites, wehrlites, clinopyroxenites, and hornblendites (Table 1). Reported olivine and clinopyroxene Mg# varied from 83.2 to 86.6 and 75 to 92, respectively. Debari *et al.* (1987) suggested

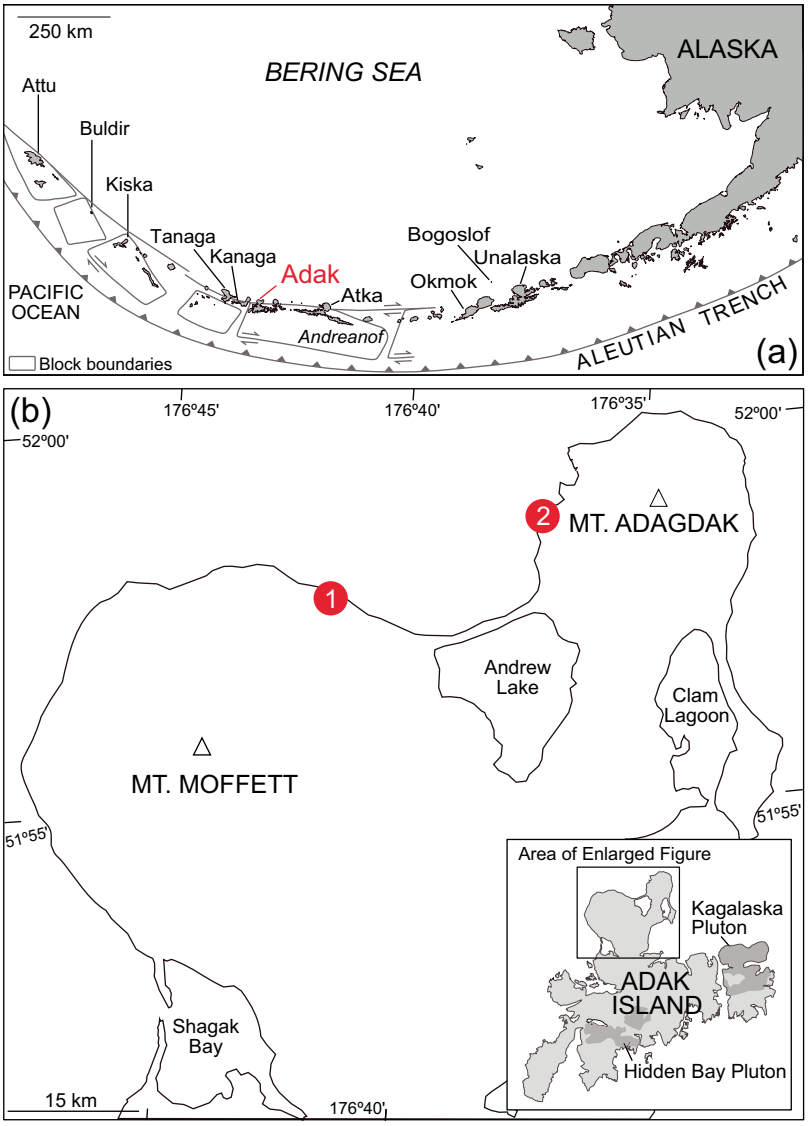

Fig. 1. a) Geological map of the Aleutian Arc. b) Enlarged map of Adak Island. The locations where the xenolith suites from 1) Mount Moffett (51°58.01′ N, 176°43.55′ W) and 2) Mount Adagdak (51°58.78′ N, 176°37.36′ W) were collected are designated with circles.

that the parental magma to these cumulates was similar to the host basalt and that the xenoliths represent the deep crustal (>0.8 GPa) cumulate complements to low-Mg, high-Al basalts typically found in the Central Aleutian arc.

Mount Moffett

Conrad *et al.* (1983) divided the xenoliths from Mount Moffett into (1) cumulate textured xenoliths, (2) cognate inclusions (*i.e.* megacrystic minerals crystallizing either within the host lava or entrained from deeper in the crust), and (3) 'composite' xenoliths (*i.e.* inclusions of quenched magmas of a different origin than the host). Conrad & Kay (1984) present mineral analyses for seven cumulate xenoliths, including two ultramafic and five gabbroic samples. In this study, we focus exclusively on cumulate xenoliths which have been classified into three petrologic groups: (1) olivine pyroxenites (±amphibole); (2) hornblende gabbros (±olivine); and (3) orthopyroxene-bearing gabbros (±olivine) (Conrad & Kay, 1984). Xenoliths in groups 1 and 2 were interpreted as part of a cogenetic crystallization sequence resulting from the differentiation of a primary hydrous basalt in the lower crust. Yogodzinski & Kelemen (2007) measured trace element abundances in clinopyroxene from two olivine clinopyroxenites (MM-102 and MM-43) (Table 1), as well as clinopyroxene phenocrysts from a magnesian andesite (MM79A) in the Cornell collection. Trace element characteristics of clinopyroxenes from Mount Moffett xenoliths, such as elevated Sr/Y and Nd/Yb ratios, resembled phenocrysts from primitive, enriched high-Mg andesites described by Kay (1978). Yogodzinski & Kelemen (2007) found that these eclogite-melt trace element characteristics were strongest in most magnesian clinopyroxenes.

METHODS

Olivine, clinopyroxene, amphibole, plagioclase, and spinel major element mineral chemistry from 46 samples from Mt. Adagdak (n = 34) and Mt. Moffett (n = 12) from the Cornell collection was obtained with a JEOL JXA-8200 electron microprobe at Caltech. Analytical conditions were a 15-kV acceleration voltage, 25 nA beam current, and a 1- to 10-μm beam diameter (1.0 μm for olivine, pyroxene, spinel, and plagioclase; 10 μm for amphibole). Detection limits for all analyzed elements were consistently

Table 1: Summary of data from previous studies of the Adak xenolith suites

Sample	Lithology	Modal abundance of cumulate phases							
		Ol	*Cpx*	*Opx*	*Spin*	*Mag*	*Amph*	*Plag*	*Glass*
Adagdak									
30	Dunite	95	4		1				
39	Dunite	92	8		minor		minor		
35	Dunite	90	9		1				
32	Wehrlite	50	50		<1		minor		
DR	Mixed dunite and clinopyroxenite	50	50		1				
ADAG81-X	Olivine clinopyroxenite	40	60		<1		minor		
34	Olivine clinopyroxenite	35	65						
8	Clinopyroxenite	2	95						3
ADG-1	Hornblendite	2				7	90	1	
ADAG82–18	Amphibolite						100		
Moffett									
MM-102	Olivine clinopyroxenite	X	X		X		X		
MM-43	Olivine clinopyroxenite	X	X				X		
MM-76BB	OPX gabbro	X	X	X		X		X	
MM-78C	OPX gabbro								
MM-78F	Hornblende gabbro		X			X	X	X	
MM-DK	Hornblende gabbro	X	X			X	X	X	
MM-7610	Hornblende gabbro		X			X	X	X	
MMG	Olivine pyroxenite	X	X		X	X	X		

Sample	Mineral chemistry				Crystallization sequence	Ref.
	Fo Ol	*Mg# CPX*	*Cr# Spin*	*Sy/Y CPX*		
Adagdak						
30	86	89	35			[1]
39	86	92	32			[1]
35	86	92	36			[1]
32	87	89	22			[1]
DR	86	88	43			[1]
ADAG81-X	83	87	27			[1]
34	86	88				[1]
8	83	86				[1]
ADG-1		75				[1]
ADAG82–18						[1]
Moffett						
MM-102	87–92	80–91	60–85	5.6–47.2	Crm, Ol + Cpx → Amph	[2, 3]
MM-43		79–91		3.8–14.6		[3]
MM-76BB	69	74			Ol → Mt, Plag, Opx + Cpx	[2]
MM-78C		74	67		Mt, Cpx + Opx, Plag + Qtz	[2]
MM-78F					Mt, Amph, Cpx + Plag	[2]
MM-DK	76–80	77–78			Mt, Ol + Cpx → Plag + Amph + Mt	[2]
MM-7610					Mt, Amph +/− Cpx, Plag	[2]
MMG	84–90	88	76		Crm, Ol + Cpx, Mt + Cpx → Amph	[2]

X = phase present. [1] Debari *et al.*, 1987; [2] Conrad & Kay, 1984; [3] Yogodzinski & Kelemen, 2007

under <0.02 wt %. For 11 of the more primitive Adagdak xenoliths, spinel compositions were analyzed separately following the methods of Wood & Virgo (1989) and recently revisited by Davis *et al.* (2017) (Supplemental Data Table S6). Each 150 to 200 spinel analyses were bracketed by analyses of standards whose $Fe^{3+}/\Sigma Fe$ ratios ($Fe^{3+}/[Fe^{3+}+Fe^{2+}]$) are known with Mössbauer spectroscopy (Wood & Virgo, 1989; Bryndzia & Wood, 1990). The bracketing procedure consisted of three core analyses from each of our 11 spinel standards. Adagdak spinels $Fe^{3+}/\Sigma Fe$ ratios were then adjusted using the Wood & Virgo (1989) correction (detailed in the Supplemental Data, Table S7). High-precision measurements of calcium in olivine cores for 15 of our most primitive xenoliths were obtained in a separate session (Supplemental Data Table S2) using a 10 kV accelerating voltage, 200 nA beam current, 10 μm spot size, and counting for 1200 seconds. Core and rim major element averages and standard deviations of olivine, pyroxene, amphibole, plagioclase, and spinel analyses are given in Supplemental Data (Tables S2-S6). Clinopyroxene, amphibole, and plagioclase trace element concentrations were obtained via Laser Ablation Inductively Coupled Plasma Mass Spectrometry (LA-ICP-MS) at Rutgers University using a Photon Machines 193 nm excimer laser coupled to a Thermo Scientific iCAPQc. All measurements represent grain cores that had previously been analyzed for their major element chemistry via electron microprobe analysis. Core trace element averages and standard deviations of clinopyroxene, amphibole, and plagioclase are given in the Supplemental Data (Tables S8-S10). A more detailed description of these methods is given in the Supplemental Data (Appendix 1).

RESULTS

A total of 59 xenoliths from Adagdak (n = 42) and Moffett (n = 17) were studied in thin section. Modal mineralogy and petrographic descriptions of each sample are given in Table 2 and Figures 2 and 3. Representative thin sections photomicrographs are presented in Figure 4. We highlight the salient features of each lithology below and provide detailed descriptions of each sample in the Supplemental Data.

Adagdak petrography

Lherzolite: ADG-CB-9 is the only lherzolite in the Adagdak sample suite. By volume, the xenolith consists of olivine (77%), clinopyroxene (14%), orthopyroxene (8%), and spinel (1%) and has a protogranular texture (Fig. 4a). Spinel occurs both interstitially and poikilitically within clinopyroxene.

Dunites: Dunites (n = 3) have protogranular textures and are composed of olivine (93–94%), spinel (3–4%), and clinopyroxene (2–3%). Spinel is present both interstitially and as poikilitic inclusions in clinopyroxene and olivine.

Wehrlites: Wehrlites (n = 8) are composed of olivine (40–83%), clinopyroxene (14–58%), and spinel (0–7%). Textures vary from adcumulate to protogranular. Clinopyroxene varies considerably in size from 0.10 to 4.5 mm across. When present, spinel is interstitial or poikilitically included in clinopyroxene or olivine (Fig. 4b).

Olivine clinopyroxenites: These xenoliths (n = 5) contain clinopyroxene (62–88%), olivine (12–37%), and spinel (~1%) and have adcumulate to protogranular textures. Except for ADG-32, which contains olivine up to 9.8 mm across, olivines in these xenoliths generally range from 0.10 to 2.2 mm in diameter. Traces of amphibole are observed as veins in samples ADG-CB-7, ADG-8, and ADG-32 along clinopyroxene grain boundaries.

Clinopyroxenites: Clinopyroxenites (n = 2) contain clinopyroxene (93–94%), olivine (5–6%), and spinel (~1%). Sample ADG-82-15 has a protogranular texture and ADG-82-1 has an adcumulate texture. Small (<10 μm) euhedral spinels are interstitial in both samples. Sample ADG-82-15 contains thin veins of amphibole along clinopyroxene grain boundaries.

Amphibole gabbros: These xenoliths (n = 19) are composed of plagioclase (8–53%), amphibole (24–64%), clinopyroxene (1–55%), Fe–Ti oxides (0–9%), and traces of olivine (0–3%), with adcumulate (n = 8) and mesocumulate (n = 11) textures. Plagioclase is generally elongate (0.10–8.0 mm long); however, three samples contain distinct poikilitic plagioclase enclosing amphibole and clinopyroxene (Fig. 4c). In most samples (n = 13), amphiboles poikilitically enclose plagioclase, clinopyroxene, and Fe–Ti oxides (Fig. 4d). Amphibole grains are generally elongate and euhedral although anhedral intercumulus amphibole is observed in sample ADG-22a. In samples ADG-4, ADG-38, ADG-73, and ADG-82-6, anhedral clinopyroxenes are surrounded by 0.2 to 1 mm amphibole rims (Fig. 4d). Most xenoliths (n = 15) contain two petrographically distinct Fe–Ti oxides populations: (1) small (10–150 μm) euhedral Fe–Ti oxides present as inclusions in amphibole or clinopyroxene, and (2) larger (0.10–1.2 mm) anhedral, interstitial Fe–Ti oxides.

Hornblendites: Hornblendites (n = 4) have modal amphibole abundances exceeding 70% and contain amphibole (79–95%), clinopyroxene (3–14%), plagioclase (0–11%), and Fe–Ti oxides (~1%). In samples ADG-26 and ADG-52, some amphiboles (~35–50%) poikilitically envelope rounded 0.1 to 1.8 mm clinopyroxenes, small (<0.02 mm) Fe–Ti oxides, or other distinct amphibole grains, while amphiboles in samples ADG-CB-10 and ADG-82-18 are mostly inclusion free. Plagioclase is only present in samples ADG-52 and ADG-CB-10, where it occurs as a continuous intercumulus fill without defined grain boundaries. Small (<0.25 mm) Fe–Ti oxides occur interstitially in all samples or as poikilitic inclusions in amphibole and clinopyroxene.

Moffett petrography

Olivine clinopyroxenites (+ amphibole): These samples (n = 6) are comprised of clinopyroxene (32–81%), olivine (9–36%), and oxide phases (0–3%) with orthocumulate textures. Samples MM-77-35, MM-77-76, and MOF-81X-G, also contain amphibole (modally 32–48%) (Fig. 4e). Amphiboles from samples MM-77-67 and MM-77-35 have 25- 125-μm-thick opaque rims (Fig. 4e). Most amphiboles (>60%) in these samples are euhedral and prismatic, although some display an intercumulus texture around pre-existing olivines and clinopyroxenes. Amphiboles from MOF-81X-G are anhedral and interstitial, often present as veins at the interface between olivine and clinopyroxene, and do not show opaque rims. MOF-81X-C and MM-77-35 contained Fe–Ti oxides and samples MM-77-67, MM-CB-2, and MOF-81X-A contain Cr-spinel.

Clinopyroxenites: These xenoliths (n = 2) have orthocumulate textures and contain clinopyroxene (90–97%) olivine (3–9%) and Fe–Ti oxides (~1%). Small Fe–Ti oxides (<40 μm) occur interstitially or as inclusions in olivine and clinopyroxene.

Amphibole gabbros: These samples (n = 4) contain plagioclase (42–68%), amphibole (23–43%), clinopyroxene (0–21%), and Fe–Ti oxides (0–10%) and show orthocumulate textures. Plagioclase in MOF-81X-D and MM-76-4 often poikilitically enclose small (<10 μm) Fe–Ti oxides or larger (50–150 μm) amphiboles or clinopyroxenes (Fig. 4f), while plagioclase from MM-76-9 and MOF-81X-F are generally inclusion free. Amphiboles from samples MM-76-4 and MOF-81X-D have 50- to 125-μm-thick opaque rims (Fig. 4f). Clinopyroxenes in MM-76-9 have experienced uralitization. When present, Fe–Ti oxides occur poikilitically.

Table 2: Summary of xenolith petrography

Sample	Phase	Mode (%)	Grain size (mm)	Description
Adagdak				
Dunites				
ADG-82-2	Olivine	94	0.1–2.2	Protogranular texture. Most spinels are observed as inclusions in cpx or olivine, interstitial spinels are rare.
	Oxide	4	0.01–0.18	
	Cpx	2	0.4–1.3	
ADG-82-21	Olivine	93	0.1–1.25	Protogranular texture. Pervasive fracturing observed throughout entire sample. Spinels <0.15 mm are generally euhedral while larger grains are anhedral.
	Cpx	4	0.15–0.8	
	Oxide	3	0.05–0.3	
ADG-63	Olivine	93	0.1–3.25	Protogranular texture. Olivines are well preserved, free of fracturing, and with clearly defined edges. About 25% of spinels show symplectic textures, the rest range from euhedral to anhedral. Clinopyroxene is subhedral to anhedral.
	Oxide	4	0.05–0.2	
	Cpx	3	0.1–0.8	
Lherzolite				
ADG-CB-9	Olivine	77	0.075–2.5	Protogranular texture. Subhedral to anhedral olivine and pyroxene. Olivines have serpentinized rims. Spinels are euhedral and interstitial.
	Cpx	14	0.15–1.375	
	Opx	8	0.25–1.2	
	Oxide	1	0.01–0.02	
Wehrlites				
ADG-CB-3	Olivine	83	0.1–0.85	Series of nested xenoliths. Innermost xenolith has adcumulate texture and is rimmed by a 7 mm thick amphibole clinopyroxenite with poikilitic amphibole.
	Cpx	14	1.1–0.2	The outer-most rim is composed of a 5 mm thin section of coarse-grained
	Oxide	3	0.01–0.1	amphibole crystals with inclusions of cpx and olivine.
ADG-30	Olivine	72	0.075–1.6	Adcumulate texture. About 50% of cpx have sieve textures. Spinels are observed
	Cpx	24	0.1–1.3	interstitially and as poikilitic inclusions. Interstitial spinels are larger than those
	Oxide	4	0.01–0.18	seen as poikilitic inclusions (0.05–0.18 mm vs 0.01–0.075 mm).
ADG-35	Olivine	50	0.12–2.1	Adcumulate texture. About 20% of cpx have sieve textures. Spinels are euhedral
	Cpx	45	0.1–1.8	and occur interstitially and as poikilitic inclusion in clinopyroxene.
	Oxide	5	0.01–0.12	
ADG-10	Cpx	52	0.2–1.45	Adcumulate texture. About 15% of cpx have sieve textures. About 65% of
	Olivine	48	0.1–1.3	olivines are anhedral, ~30% are subhedral, and ~5% are euhedral. The euhedral
	Oxide	trace	0.01–0.1	grains are smaller (0.1–0.2 mm) and primarily occur as inclusions in cpx.
ADG-33	Cpx	53	0.15–4.5	Protogranular texture. No grains in sample contain poikilitic inclusion or display
	Olivine	47	0.1–1. 75	sieve textures.
ADG-82-3	Cpx	58	0.2–2.3	Protogranular texture. Sieve textures or poikilitic inclusions of olivine and spinel
	Olivine	42	0.05–1.5	are observed in cpx > 1 mm. Euhedral spinels seen interstitially and as poikilitic
	Oxide	< 1	<0.01–0.05	inclusions in cpx and olivine.
ADG-CB-5	Cpx	58	0.1–6	Adcumulate texture. Clinopyroxenes show pervasive fracturing and partially
	Olivine	42	0.05–1.7	reabsorbed rims. Larger olivines (> 1 mm) often contain inclusions of smaller
	Oxide	< 1	0.01–0.05	olivines. Spinel observed interstitially and as poikilitic inclusions in cpx.
ADG-42	Cpx	53	0.2–2	Protogranular texture. Subhedral to anhedral cpx and euhedral olivine. Spinels
	Olivine	40	0.1–0.8	occur as poikilitic inclusions in cpx.
	Oxide	7	0.01–0.2	
	OPX	< 1 (n = 2)	1.5–3	
Olivine clinopyroxenites				
ADG-82-17	Cpx	62	0.17–2.4	Adcumulate texture. Olivine and cpx are generally free of fracturing and
	Olivine	37	0.1–2.1	crystalline edges are well preserved.
	Oxide	1	< 0.1	
ADG-32	Cpx	68	1.25–19.3	Protogranular texture. Larger cpx (> 10 mm) are euhedral and smaller grains
	Olivine	32	0.1–9.8	(< 4 mm) are subhedral to anhedral. Spinels are observed interstitially and as
	Oxide	< 1	0.6–2.1	poikilitic inclusions in cpx and olivine.
ADG-CB-7	Cpx	74	0.08–0.9	Protogranular texture. Clinopyroxenes are subhedral to anhedral and olivines
	Olivine	25	0.1–1.1	are euhedral. Small euhedral spinels are seen interstitially.
	Oxide	1	< 0.01	
DR	Cpx	87	0.2 to 4.2	Protogranular texture. Clinopyroxene is subhedral to anhedral and sometimes
	Olivine	13	0.1 to 2.2	contains small (0.2–0.35 mm) inclusions of rounded olivine grains. Spinels are
	Oxide	< 1	0.01–0.05	euhedral and seen interstitially.
ADG-8	Cpx	88	0.22–2.5	Adcumulate texture. About 50% of cpx have sieve textures. Most Fe–Ti oxides
	Olivine	12	0.15–0.6	(> 90%) are present as poikilitic inclusions in cpx. In some areas, skeletal
	Oxide	< 1	0.01–0.18	olivines fill the space between cpx grains.

(Continued)

Table 2: Continued

Sample	Phase	Mode (%)	Grain size (mm)	Description
Clinopyroxenites				
ADG-82-1	Cpx	93	0.1–3	Adcumulate texture. Clinopyroxene and olivine along the rim of the sample (outer 2–6 mm) show sieve textures. Most olivines are euhedral, although several skeletal olivines also observed. Small euhedral spinels seen interstitially.
	Olivine	6	0.1–1.2	
	Oxide	1	< 0.01	
ADG-82-15	Cpx	94	0.1–3.2	Protogranular texture. Clinopyroxenes sometimes contain inclusions of olivine with serpentinized rims or smaller distinct cpx. Small euhedral spinels observed interstitially.
	Olivine	5	0.1–0.2	
	Oxide	1	0.01	
Amphibole gabbros				
ADG-77	Amph	24	0.4–1.7	Mesocumulate texture. Plagioclase is subhedral and individual grains interlock one another. Amphibole occurs poikilitically. All cpx have sieve textures and > 90% contain poikilitic inclusions of Fe–Ti oxides. All cpx show reabsorption along their rims. Oxides are subhedral to anhedral and occur interstitially and as inclusions in cpx and amphibole. Oxides with symplectic textures also observed. Olivines >0.25 mm are usually skeletal. Smaller olivines are seen both interstitially and as inclusions in amphibole and cpx.
	Plag	51	0.1–1.3	
	Cpx	19	0.2–1.4	
	Oxide	3	0.1–0.7	
	Olivine	3	0.1–0.6	
ADG-24	Plag	43	0.25–4.7	Mesocumulate texture. About 50% of amphiboles >3 mm occur poikilitically and contain inclusions of plagioclase, cpx, and olivine. About 70% of cpx contain inclusions of Fe–Ti oxides, amphibole, and/or plagioclase. Small euhedral oxides (0.075 to 0.15 mm) are present as poikilitic inclusions in other phases. Larger oxides are generally anhedral.
	Amph	38	0.3–5	
	Cpx	12	0.2–3	
	Oxide	4	0.075–0.7	
	Olivine	3	0.1–1.1	
ADG-CB-1	Cpx	55	0.15–2.25	Adcumulate texture. Clinopyroxene often contains inclusions of olivine, amphibole, and Fe–Ti oxides. Small amphiboles (<1 mm) are euhedral/subhedral and larger grains (>2 mm) occur poikilitically around cpx, plag, olivine, and other distinct amphiboles. Intercumulus plag contains olivine and cpx inclusions. Small euhedral Fe–Ti oxides (0.01 to 0.1 mm) present as inclusions in cpx. Larger anhedral Fe–Ti oxides (0.15 to 0.6 mm) appear as intercumulus phases.
	Amph	30	0.2–7	
	Plag	8	0.1–0.8	
	Oxide	5	0.01–0.6	
	Olivine	2	0.02–0.75	
ADG-22	Plag	40	0.2–8	Mesocumulate texture. Amphiboles occur poikilitically around large (0.25–1.5 mm) plagioclase, cpx, and distinct amphiboles. Poikilitic amphiboles range from 9 mm to 1.5 cm in diameter, but 40–70% of their area is occupied by other phases. Approximately 20% of all cpx are skeletal and all cpx show partially reabsorbed rims. Fe–Ti oxides <0.25 mm are euhedral and grains between 0.25–0.6 mm are subhedral or anhedral.
	Amph	39	—	
	Cpx	15	0.3–2.75	
	Oxide	4	0.02–0.6	
	Olivine	2	0.25–1.2	
ADG-73	Amph*	42	0.3 - 1.9	Adcumulate texture. > 80% of amphiboles occur poikilitically around Fe–Ti oxides, plag, cpx, and/or olivine. About 85% of plag have sieve textures and ~5% contain poikilitic inclusions small oxides (< 0.01 mm) or amphiboles (0.02 and 0.06 mm). About 30% of all cpx over 1 mm in diameter are skeletal.
	Plag	41	0.075–0.8	
	Cpx	12	0.2–1.3	
	Oxide	3	0.03–0.6	
	Olivine	2	0.1–0.35	
ADG-19	Amph	41	0.1–2.3	Mesocumulate texture. Amphiboles are euhedral and about 60% contain inclusions of plag, cpx, and/or Fe–Ti oxides. Small euhedral Fe–Ti oxides (0.05–0.1 mm) occur as poikilitic inclusions in cpx and amphibole and larger anhedral grains (>0.12 mm) appear as intercumulus phases.
	Plag	40	0.1–2.1	
	Cpx	12	0.1–2.1	
	Oxide	5	0.05–0.5	
	Olivine	2	0.15–0.3	
ADG-82-6	Amph*	39	—	Mesocumulate texture. Amphiboles occur as intercumulus phases or poikilitically and do not show distinct grain boundaries. Poikilitic amphiboles contain inclusions of 0.1–0.4 mm plag, cpx, olivine, and distinct euhedral amphiboles. Clinopyroxenes pervasively show sieve textures and partially reabsorbed rims. Many cpx (> 65%) contain poikilitic inclusions of small (0.02 to 0.1 mm) Fe–Ti oxides. Larger oxides (0.1–0.2 mm) are present interstitially. Olivines occur as inclusions in amphibole.
	Plag	26	0.1–0.8	
	Cpx	30	0.2–0.7	
	Oxide	4	0.02–0.2	
	Olivine	1	0.15–0.2	
ADG-38	Plag	44	0.2–0.9	Mesocumulate texture. Plagioclase is lath-like and > 95% of grains have sieve textures. Amphiboles are anhedral and do not show distinct grain boundaries. About 70% of amphiboles occur poikilitically around Fe–Ti oxides, plag, cpx, and olivine. Fe–Ti oxides show a great diversity of sizes and morphologies. About 20% of oxides have symplectic texture. Olivine is primarily present as inclusions in amphibole.
	Amph*	37	—	
	Cpx	14	0.2–1.1	
	Oxide	4	0.01–0.3	
	Olivine	1	0.1–0.2	
ADG-6	Amph	56	0.1–1.1	Mesocumulate texture. ~ 80% of amphiboles occur poikilitically around Fe–Ti oxides, plag, cpx, and olivine. Small cpx (0.1–0.25 mm) only present as inclusions in amphibole. Larger cpx (>0.25 mm) contain inclusions of Fe–Ti oxides and olivine. Larger oxides (> 0.25 mm) are subhedral to anhedral and appear as intercumulus phases. Smaller euhedral oxides (0.02–0.2 mm) are observed as inclusions in cpx and amphibole.
	Plag	28	0.2–1.2	
	Cpx	11	0.1–1.1	
	Oxide	4	0.02–0.9	
	Olivine	1	0.075–1	

(Continued)

Table 2: Continued

Sample	Phase	Mode (%)	Grain size (mm)	Description
ADG-74	Plag	48	0.08–1	Adcumulate texture. Amphiboles <0.4 mm are hexagonal and euhedral. Larger amphiboles (0.4–1.8 mm) are anhedral and occur poikilitically around cpx, plag, Fe–Ti oxides, and olivine. About 70% of plagioclase have sieve textures.
	Amph	41	0.2–1.8	Clinopyroxene contains poikilitic inclusions of Fe–Ti oxides. Oxides between 0.1
	Cpx	8	0.15–0.8	and 0.12 are euhedral and present as inclusions in other phases. Larger
	Oxide	3	0.1–0.25	anhedral oxides (<0.25 mm) are interstitial. Olivine is only present as inclusions
	Olivine	< 1	0.1–0.4	in amphibole or cpx.
ADG-4	Amph*	49	—	Mesocumulate texture. Amphiboles occur poikilitically or as rims around other
	Plag	43	0.17–2.1	phases. Most cpx (> 90%) contain poikilitic inclusions of smaller (0.2–0.1 mm)
	Cpx	5	0.1–1.1	euhedral oxides. Small (0.01–0.05 mm) euhedral Fe–Ti oxides are present as
	Oxide	3	0.01–0.7	poikilitic inclusions in cpx and amphibole. Larger (0.25–0.7 mm) anhedral oxides
	Olivine	< 1	0.15–0.3	are seen interstitially.
ADG-17	Amph	29	0.15 to 8	Mesocumulate texture. Most (> 90%) amphiboles over 2.25 mm occur
	Plag	51	0.1–0.75	poikilitically and contain inclusions of oxides, plagioclase, and cpx. About 90%
	Cpx	18	0.15–1.1	of oxides are anhedral, 0.1 and 0.25 mm in diameter, and occur interstitially.
	Oxide	2	0.05–0.3	Smaller euhedral oxides (< 0.1 mm) are only seen as poikilitic inclusions.
ADG-CB-2	Amph	64	0.25–4.9	Mesocumulate texture. About 20% of amphiboles contain inclusions of smaller distinct amphiboles or cpx. Twelve large poikilitic grains of plagioclase were noted in this sample, ranging from 2.5 to 5.2 mm in diameter, each containing between 15 and 30 grains of amphibole and cpx. 5% of Fe–Ti oxides show symplectic textures.
	Plag	21	0.1–5.1	
	CPX	12	0.15–1.3	
	Oxide	3	0.01–0.8	
ADG-5	Amph	44	0.3–3.2	Adcumulate texture. Amphiboles are euhedral to subhedral and ~20% have
	Plag	37	0.2–1.8	0.02 to 0.03 mm thick opaque rims. Plagioclase is anhedral. All cpx have sieve
	Cpx	10	0.18–1.25	textures and about 20% are skeletal. Fe–Ti oxides are anhedral.
	Oxide	9	0. 1–1	
ADG-CB-6	Plag	48	0.025–0.7	Adcumulate texture. About 5% of plagioclase contain inclusions of amphibole or cpx. About 50% of amphiboles occur poikilitically and contain inclusions of Fe–Ti oxides, plag, or cpx. All cpx have partially reabsorbed rims and ~30% are
	Amph	37	0.1–1.9	skeletal in form. Small euhedral Fe–Ti oxides (<0.01–0.15 mm) occur as poikilitic
	Cpx	9	0.075–0.2	inclusions in amphibole and larger anhedral oxides (0.075–0.4 mm) are seen
	Oxide	6	0.075–0.35	interstitially.
ADG-82-5	Amph	50	0.1–1.2	Adcumulate texture. Amphiboles are generally elongated. About 60% of
	Plag	38	0.07–1.3	plagioclase over 0.8 mm in length occurs poikilitically around small (< 0.25 mm)
	Cpx	6	0.05–0.3	amphiboles. Clinopyroxenes show partially reabsorbed rims. Subhedral Fe–Ti
	Oxide	6	0.02–0.55	oxides.
ADG-CB-4	Plag	46	0.07–2.25	Mesocumulate texture. Smaller plag (< 0.3 mm) is euhedral/subhedral and larger grains are anhedral and intercumulus, often containing inclusions of
	Amph	43	0.1–2.75	amphibole and cpx. Small euhedral Fe–Ti oxides (0.025–0.075 mm) present as
	Cpx	6	0.08–0.45	poikilitic inclusions in amphibole and cpx while larger anhedral oxides
	Oxide	5	0.025–1.2	(0.2–1.2 mm) are observed as intercumulus phases.
ADG-29	Amph	51	0.3–1.1	Adcumulate texture. Slight metamorphic fabric, with elongate plagioclase and
	Plag	39	0.08–0.25	amphibole grains consistently aligning along the same plane. Most amphiboles
	Cpx	6	0.15–0.5	(> 90%) have sieve textures and ~50% contain cpx inclusions. Individual
	Oxide	4	0.08–0.4	plagioclase grains are anhedral and interlocking with one another.
ADG-7	Plag	53	0.1–3.4	Adcumulate texture. About 40% of amphiboles have opaque rims between
	Amph	42	0.5–9	0.025–0.05 mm thick and 80% have sieve textures. Most oxides (> 95%) are
	Oxide	4	0.01–1	anhedral and > 0.1 mm. Small (0.01–0.02 mm) euhedral oxides present as
	Cpx	1	0.2–0.4	poikilitic inclusions in plag, amphibole, and cpx.
Hornblendites				
ADG-26	Amph	93	0.15–3	Mesocumulate texture. Amphiboles <1.5 mm in length are generally hexagonal,
	Cpx	6	0.25–0.7	and those >2 mm long are elongated. Olivine present as poikilitic inclusions in
	Olivine	< 1	0.075–0.8	amphibole.
	Oxide	1	0.01–0.02	
ADG-82-18	Amph	98	0.25–3.25	Orthocumulate texture. Euhedral hexagonal amphiboles. Clinopyroxene and
	Cpx	2	0.2–1.3	olivine are rare and highly altered when present, with pervasive fracturing and
	Olivine	<1	0.2–0.8	partially reabsorbed rims. Fe–Ti oxides seen interstitially or as inclusions in
	Oxide	<1	<0.01	amphibole.
ADG-52	Amph	82	0.15–2.75	Adcumulate texture. Contains both euhedral and poikilitic amphiboles.
	Cpx	14	0.1–1.8	Euhedral amphiboles have partially reabsorbed rims and pervasive fracturing, while poikilitic grains are well preserved. Clinopyroxenes contain inclusions of
	Plag	4	—	spinel. Plagioclase appears only as an intercumulus phase filling void space
	Oxide	<1	0.02	between amphibole and cpx and does not show distinct grain boundaries

(Continued)

Table 2: Continued

Sample	Phase	Mode (%)	Grain size (mm)	Description
ADG-CB-10	Amph	79	0.1–2.5	Mesocumulate texture. Elongate and fractured amphiboles with inclusions of cpx. Plagioclase only observed as an intercumulus phase. Clinopyroxenes have sieve textures. Oxides observed interstitially.
	Plag	11		
	Cpx	9	0.05–1.9	
	Oxide	1	0.025–0.25	
Moffett				
Olivine clinopyroxenites				
MOF-81X-A	Cpx	64	0.16–0.9	Orthocumulate texture. Clinopyroxene contains small inclusions of serpentinized olivine. Cr-spinels occur interstitially and as poikilitic inclusions in cpx and olivine
	Olivine	36	0.1–0.6	
	Oxide	<1	<0.05	
MM-CB-2	CPX	66	0.12–2.25	Orthocumulate texture. Clinopyroxene >0.25 mm in diameter occurs poikilitically, each containing 3 to ~40 small (>150 μm) inclusions of olivine and distinct cpx. Olivines have serpentinized rims and often occur as inclusions in cpx.
	Olivine	34	0.05–0.5	
	Oxide	<1	<0.01	
MOF-81X-C	Cpx	81	0.16–01.1	Orthocumulate texture. Euhedral to subhedral cpx, often with partially reabsorbed rims. About 60% of cpx have sieve textures. Fe–Ti oxides occur interstitially or as poikilitic inclusions in cpx.
	Olivine	18	0.1–0.75	
	Oxide	1	0.12–0.04	
Olivine clinopyroxenites (+ amphibole)				
MM-77-67	Amph	48	0.25–1.3	Orthocumulate texture. Amphiboles occur both as euhedral inclusion-free grains and against olivine/cpx grain boundaries. Amphiboles have 0.05–0.13 mm opaque rims. About 75% of cpx and anhedral and 25% are euhedral. The Euhedral cpx show oscillatory zoning. Olivine and Fe–Ti oxides occur as inclusions in cpx or amphibole.
	Cpx	32	0.125–1	
	Olivine	17	0.08–0.9	
	Oxide	3	0.02–0.08	
MOF-81X-G	Cpx	51	0.17–2.25	Adcumulate texture. Most cpx are highly fractured but those that are not show oscillatory zoning. Clinopyroxenes contain inclusions of olivine and Fe–Ti oxides. Most amphiboles (~90%) are anhedral and appear as an interstitial phase or poikilitically around cpx or olivine.
	Amph*	33	0.31–7	
	Olivine	16	0.05–0.46	
MM-77-35	Amph	46	0.32–1.75	Orthocumulate texture. Amphiboles occur both as euhedral grains without inclusions and poikilitically around 0.1 to 0.25 mm olivine and cpx. Clinopyroxenes show oscillatory zoning and are euhedral to subhedral. All Fe–Ti oxides occur as poikilitic inclusions in cpx or amphibole.
	Cpx	44	0.15–1.13	
	Olivine	9	0.075–1.25	
	Oxide	1	0.025–0.075	
Clinopyroxenites				
MM-CB-3	Cpx	90	0.6–2.4	Orthocumulate texture. Euhedral olivine and cpx, about half display sieve texture. Fe–Ti oxides occur interstitially or as poikilitic inclusions in cpx and olivine.
	Olivine	9	1.1	
	Oxide	1	< 0.04	
MOF-81X-B	Cpx	97	0.1–1.5	Orthocumulate texture. Euhedral to subhedral cpx, some with embayed rims. About half of all cpx contain poikilitic inclusions of olivine or small (0.01–0.05 mm) oxides.
	Olivine	3	0.07–0.12	
	Oxide	<1	< 0.02	
Amphibole gabbros				
MM-76-4	Plag	42	0.25–2.4	Orthocumulate texture. Subhedral plag. All amphiboles have 0.05–0.075 mm thick opaque rims. Skeletal cpx. One grain of skeletal olivine ~1.2 mm in diameter observed. Fe–Ti oxides occur interstitially and as intercumulus phases.
	Amph	27	0.2–2.6	
	Cpx	21	0.4–1.6	
	Oxide	10	0.05–0.8	
MOF-81X-F	Plag	68	0.15–1.25	Orthocumulate texture. Most amphiboles have 0.01–0.025 mm opaque rims. Clinopyroxenes are pervasively fractured with partially reabsorbed edges, sometimes showing sieve textures. Fe–Ti oxides are euhedral and observed as inclusion in amphibole.
	Amph	23	0.17–1.3	
	Cpx	9	0.3–1.75	
MOF-81X-D	Plag	49	0.2–1.2	Orthocumulate texture. Plagioclase often contains poikilitic inclusions of small oxides (< 0.01 mm) or larger (0.05–0.15 mm) grains of amphibole, cpx, or distinct plagioclases. All amphiboles have 0.075 to 0.15 mm thick opaque rims. Clinopyroxenes show sieve textures.
	Amph	41	0.2–1.4	
	Cpx	7	0.1–0.3	
	Oxide	3	0.025–0.3	
MM-76-9	Plag	55	0.15–0.5	Orthocumulate texture. Plagioclase is euhedral to subhedral. Oxides only observed as poikilitic inclusions in amphibole. Clinopyroxenes have experienced almost complete uralitization.
	Amph	43	0.25–2.5	
	Oxide	2	<0.05	

(Continued)

Table 2: Continued

Sample	Phase	Mode (%)	Grain size (mm)	Description
Hornblendites				
MM-77-100	Amph	90	0.2–1.7	Orthocumulate texture. Plagioclase is equigranular. Clinopyroxenes show sieve textures. Olivine and cpx usually observed as inclusions in amphibole.
	Cpx	4	0.1–0.5	
	Plag	4	0.1–0.25	
	Olivine	2	0.07–0.35	
MM-77-61	Amph	74	0.3–3.5	Mesocumulate texture. Amphiboles are pervasively fractured and have 0.05 to 0.1 mm thick opaque rims. Clinopyroxene is observed both as small (0.2 to 0.5 mm) euhedral to subhedral zoned grains and as larger (0.75–1.5 mm) fractured grains with embayed rims. Euhedral Fe–Ti oxides.
	Cpx	16	0.2–1.5	
	Plag	7	0.125–1.75	
	Oxide	3	0.025–0.1	
MOF-81X-E	Amph	91	0.3–11	Orthocumulate texture. Most amphiboles have 0.01–0.025 mm thick opaque rims. Clinopyroxenes and Fe–Ti oxides only observed as inclusion in amphibole. Clinopyroxenes are pervasively fractured and have partially reabsorbed edges, sometimes showing sieve textures. Fe–Ti oxides are euhedral.
	Cpx	5	0.075–0.5	
	Oxide	4	0.01–0.075	
MM-77-29	Amph	86	0.25–3.75	Mesocumulate texture. About half of all amphiboles have 0.05 and 0.1 mm thick opaque rims. Cpx, opx, and olivine usually observed as poikilitic inclusions in amphibole. Fe–Ti oxides only present as inclusions in amphibole or pyroxene.
	Plag	5	0.2–1.3	
	Cpx	5	0.075–1.8	
	Opx	3	0.1–0.4	
	Oxide	1	0.015	
	Olivine	<1	<0.1	
MM-CB-1	Amph	99	0.1–9	Orthocumulate texture. Most amphiboles have 0.01 mm thin opaque rims. Cracks in amphiboles filled with fine-grained plagioclase and Fe–Ti oxides. Fine to medium-grained plagioclase occasionally fills intercumulus spaces between amphibole grains.
	Plag	1	0.17–1	
	Olivine	<1 (n = 1)	0.75	

More detailed descriptions of each sample are given in the Supplemental Data Amph, amphibole; plag, plagioclase; cpx, clinopyroxene; cpx, orthopyroxene
*Petrography suggests amphibole may be peritectic in nature

Hornblendites: Moffett hornblendites (n = 5) contain amphibole (74–99%), clinopyroxene (0–16%), plagioclase (0–7%), and Fe–Ti oxides (0–4%) and show mesocumulate to orthocumulate textures. Amphibole is highly altered, especially along cleavage planes, with pervasive fracturing observed in all grains. Opaque rims (10–25 μm thick) are observed in amphiboles from samples MM-CB-1 and MOF-81X-E.

Adagdak major and trace element mineral chemistry

Olivine: Sample average Mg# ($[Mg/(Mg + Fe^T)] \times 100$ for all phases but spinel) for olivine cores ranges from 84.1 to 87.1 for ultramafic Adagdak cumulates (Fig. 5a). Lherzolite ADG-CB-9 and amphibole gabbro ADG-CB-1 have average olivine core Mg# of 91.3 and 73.5, respectively (Fig. 5a). Including literature data, average core NiO concentrations positively correlate with Mg# and range from 0.03 to 0.30 wt % (Fig. 5a). In samples analyzed for high-precision Ca-in-olivine (n = 13), core Ca concentrations range from 290 to 645 μg/g (0.04 to 0.09 wt % CaO). Core-to-rim zoning was only observed in the more evolved samples (amphibole gabbros, clinopyroxenites, and olivine clinopyroxenites), with Mg# typically decreasing by 0.5 to 1.0 from core to rim.

Pyroxene: Clinopyroxene is the only phase present throughout the entire Adagdak suite and consists predominantly of diopside. Sample average Mg# of clinopyroxene cores ranges from 93.8 to 81.6 for the ultramafic xenoliths and from 73.6 to 77.8 in the amphibole gabbros and hornblendites) (Fig. 5b, c). $K_{Ol-CPX}^{Fe^T/Mg}$ (molar $\frac{(Fe^T/Mg)_{Ol}}{(Fe^T/Mg)_{CPX}}$) varies from 0.77 to 1.53 (Fig. 5b). Average Al_2O_3 concentrations range from 1.34 to 5.44 wt % in the ultramafic lithologies and reach their highest values in the hornblendites (6.9–8.5 wt %; Fig. 5c). All clinopyroxenes are depleted in Nb and Ta with negative Zr anomalies ($Zr/Zr* = Zr_N/[Nd_N \times Sm_N]^{0.5}$, where N designates normalization to CI chondrites; McDonough & Sun, 1995), which range from 0.2 to 0.6 and are negatively correlated with Mg#. Eu-anomalies ($Eu/Eu* = Eu_N/[Sm_N \times Gd_N]^{0.5}$) are not observed in Adagdak xenolith clinopyroxenes (Fig. 6). Sr anomalies ($Sr/Sr* = Sr_N/[Pr_N \times Nd_N]^{0.5}$) correlate positively with Mg# and are generally positive (>1) in the ultramafic lithologies (0.96–2.18) and negative (<1) in clinopyroxenes from the amphibole gabbros and hornblendites (0.61–0.74) (Fig. 7a). Clinopyroxene Sr/Y and La/Yb ratios positively correlate with Mg# and vary from 3.4 to 21.3 and from 0.5 to 2.7, respectively (Fig. 7b).

Amphibole: Average amphibole core Mg# ranges from 64.3 to 71.3 and does not correlate with rock type or the concentration of any major element. Seven of the Adagdak amphibole gabbros contain magnesio-hastingsite and one contains pargasitic amphibole (based on the nomenclature of Leake *et al.*, 2004). All Adagdak hornblendites contain pargasitic amphibole. Amphiboles are consistently enriched in Cs, Rb, Ba, and Sr (Sr/Sr* 1.9–8.8: Supplemental Data Figure S2).

Plagioclase: Plagioclase in the Adagdak amphibole gabbros and hornblendites are anorthite-rich (An_{91-96}) and unzoned. Plagioclase is consistently enriched in LREE and LILE, particularly Sr (530–830 μg/g) relative to the HREE (La/Yb 0.1–0.3) and HFSE. All samples show positive Ba, Pb, Sr, and Eu anomalies on primitive mantle normalized spider diagrams (McDonough & Sun, 1995) (Supplemental Data Figure S3).

Spinel: Average Cr# (100*molar Cr/[Cr + Al]) from spinel cores ranges from 4 to 60 and decreases with increasing Mg# (for spinel only, we define Mg# as $[Mg/(Mg + Fe^{+2})] \times 100$) (Fig. 5d). Spinel core Cr# for olivine clinopyroxenite, wehrlite, and dunite xenoliths ranges from 22.3 and 47.0. Lower Cr#s, ranging from 0.4 to 11, are observed in amphibole gabbro and clinopyroxenite xenoliths. Average core Mg# varies from 50.4 to 72.9 in the Adagdak suite. Calculated sample average $Fe^{3+}/\Sigma Fe$ ratios from spinel cores range from 0.3 to 0.5 and do not correlate with Mg#, Cr#, (Fig. 5e) nor the concentration of any major oxide. Magnetite is

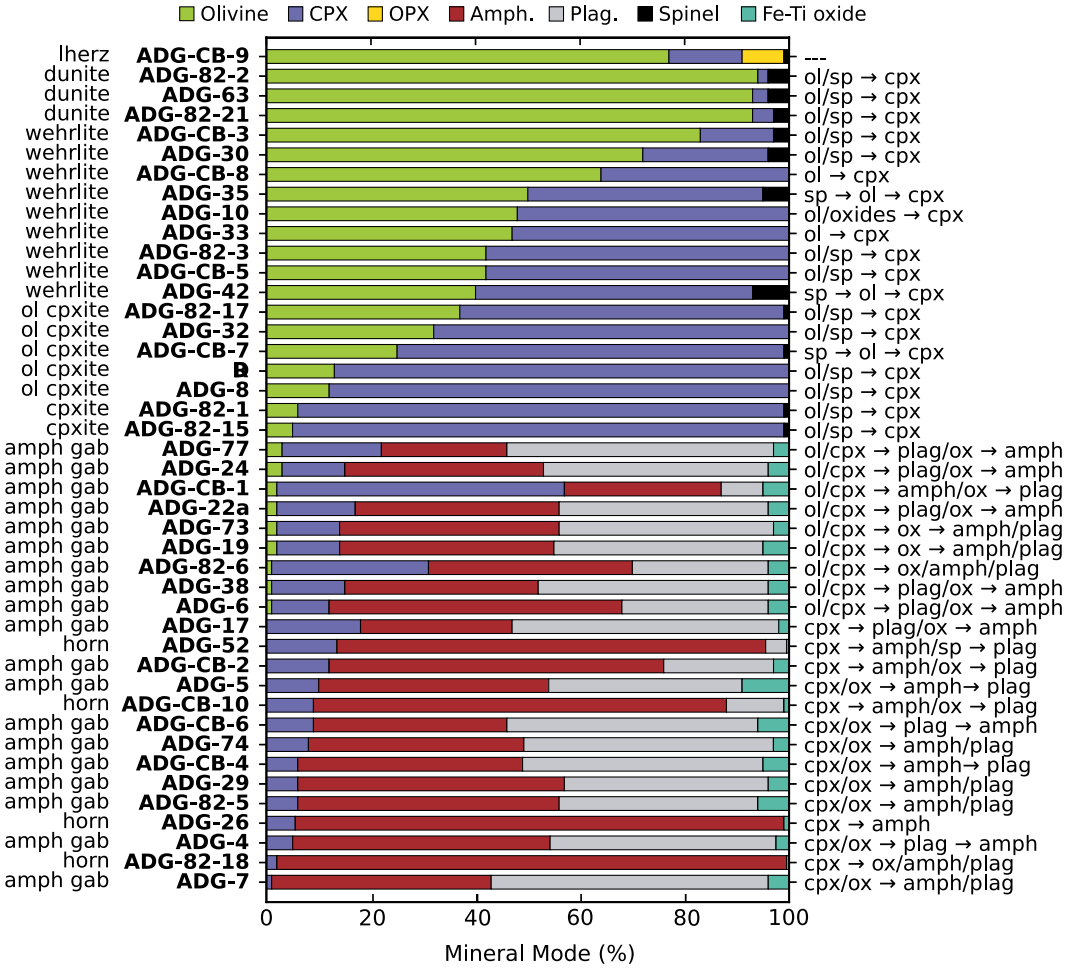

Fig. 2. Adagdak xenolith modal proportions (in vol. %). Crystallization sequence for cumulate samples is based on petrographic relationships observed in thin section. *Lherz* lherzolite, *ol cpxite* olivine clinopyroxenite, *amph gab* amphibole gabbro, *horn* hornblendite.

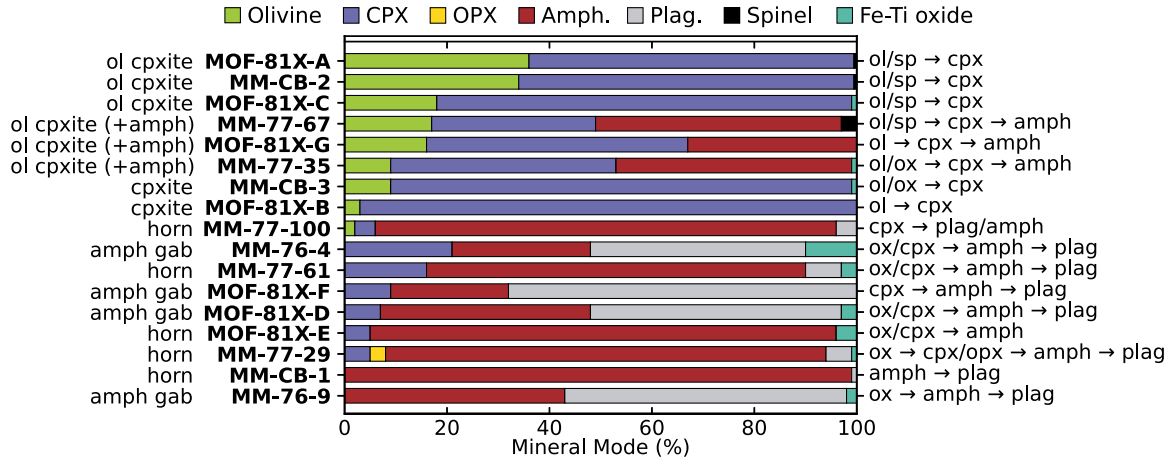

Fig. 3. Moffett xenoliths modal proportions (in vol. %). Abbreviations are the same as in Figure 2.

the dominant oxide in the more evolved amphibole gabbro and hornblendite cumulates.

Moffett major and trace element mineral chemistry

Olivine: Olivine core Mg# and NiO range from 84.8 to 89.0 and from 0.13 to 0.23 wt %, respectively (Fig. 5a). Normal zoning in Mg# is observed in the outer 20 to 60 μm rims of olivine from samples MM-77-35 and MOF-81X-C. Reverse zoning is only observed in olivine from sample MOF-81X-A, where the outer 50 μm rims show increased Mg# adjacent to clinopyroxene. Calcium concentrations (750–970 μg/g) are higher in olivines from Moffett than in those for Adagdak and do not correlate with Mg# or major element concentration.

Pyroxenes: Clinopyroxenites (±olivine) have clinopyroxene core Mg# between 88.5 and 90.7. Clinopyroxene consists of diopside

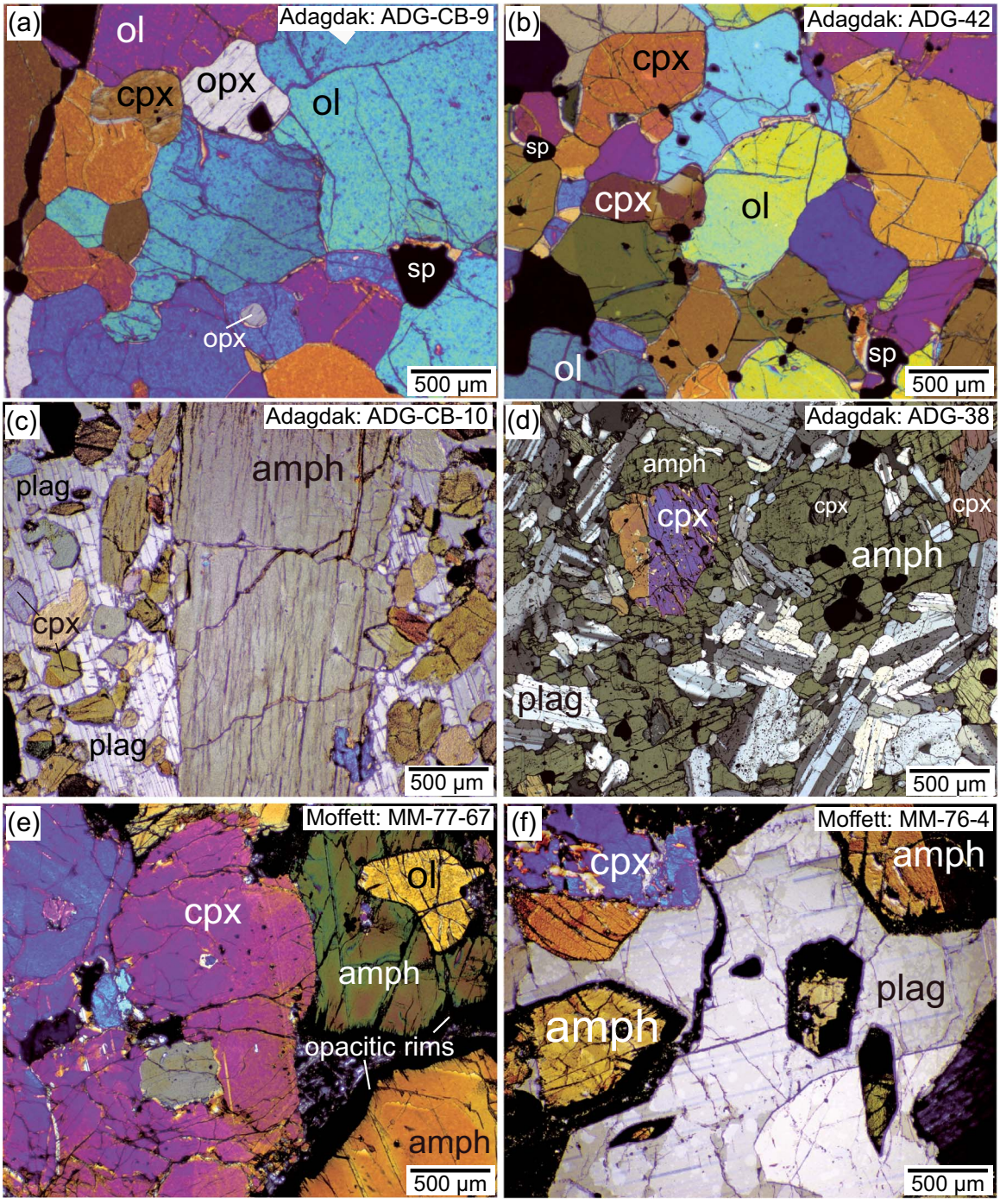

Fig. 4. Photomicrographs of thin sections in cross-polarized light. (a) Adagdak lherzolite ADG-CB-9. (b) Adagdak wehrlite ADG-42. (c) Adagdak hornblendite ADG-CB-10. (d) Adagdak amphibole gabbro ADG-38. (e) Moffett amphibole-bearing olivine clinopyroxenite MM-77-67. f) Moffett amphibole gabbro MM-76-4.

in all samples except olivine clinopyroxenite MOF-81X-C, which contains augite. Clinopyroxene Mg# in the amphibole-bearing samples ranges from 72.7 to 78.1. Sample average Al_2O_3 concentrations range from 1.1 to 8.0 wt % and negatively correlate with Mg# (Fig. 5c). Sample $K_{Ol-CPX}^{Fe^T/Mg}$ ranges from 0.70 to 1.88 (Fig. 5b). Strontium anomalies range from 0.7 to 2.8 and positively correlate with Mg# (Fig. 7a). Sample average Sr/Y and La/Yb ratios positively correlate with Mg# and range from 6.4 to 41.7 and from 1.2 to 2.5, respectively (Fig. 7b, c). All samples are depleted in LREE and HREE relative to MREE (Fig. 8).

Amphibole: Samples MM-77-35 and MM-77-67 contain populations of both euhedral and intercumulus amphiboles. In both samples, the major element chemistry of the two groups is similar (Table S4). All Moffett samples contain magnesio-hastingsite except for samples MM-CB-1 and MOF-81X-G, which contain pargasitic amphibole. We do not observe the high Cr concentrations Conrad & Kay (1984) reported for amphiboles from ultramafic xenoliths (up to 0.55 wt % Cr_2O_3), with Cr_2O_3 concentrations in the amphiboles cores we analyzed never exceeding 0.07 wt %. Amphiboles are enriched in Sr and Ba and depleted in the LREE

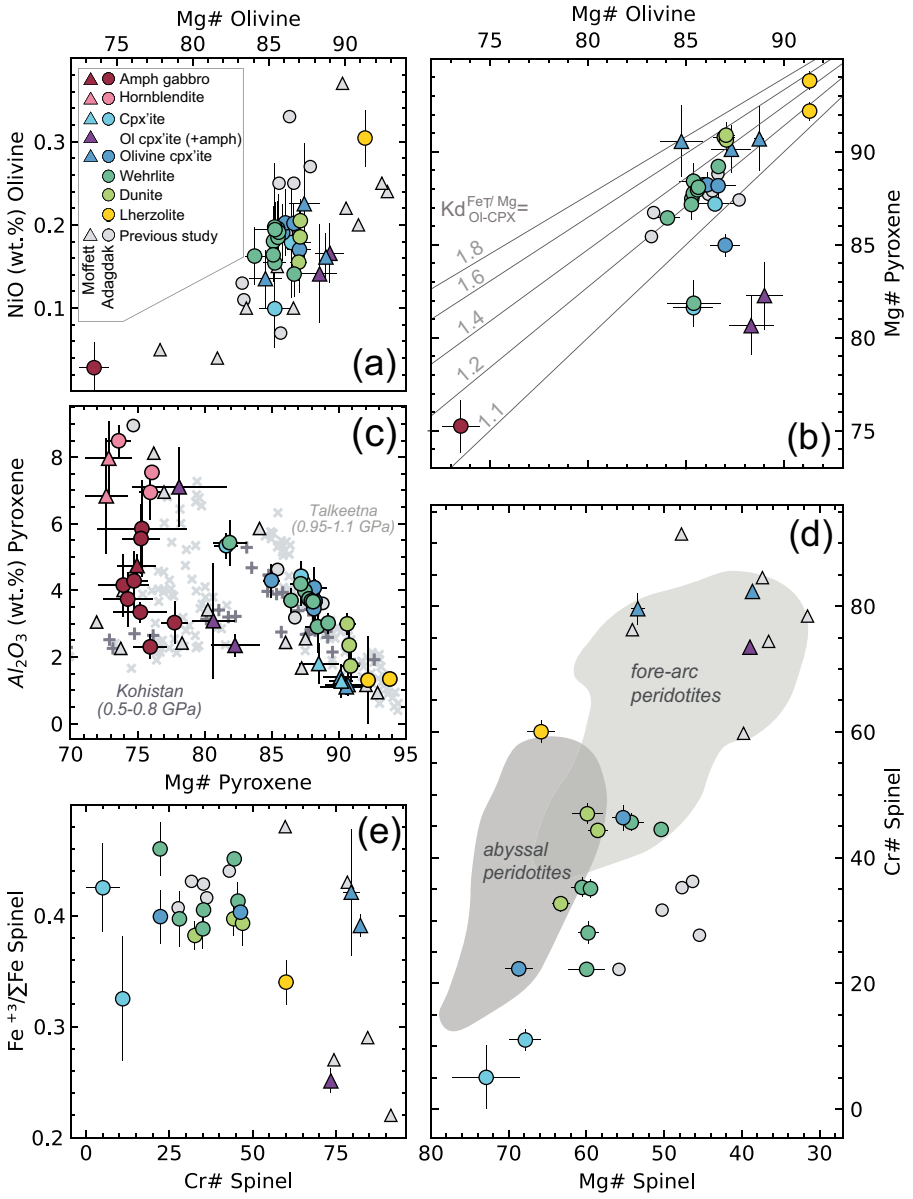

Fig. 5. Summary of xenolith major element mineral chemistry. Error bars represent 2σ variations in sample composition. (a) Olivine Mg# vs. NiO_2 (wt %). (b) Olivine Mg# vs. clinopyroxene Mg#. (c) Pyroxene Mg# vs. Al_2O_3 (wt %). Clinopyroxene data from the Chilas complex, Kohistan (Jagoutz *et al.*, 2007), and Talkeetna (Beyer, 1980; DeBari & Coleman, 1989; Greene *et al.*, 2006) is given for comparison. (d) Spinel Mg# vs. Cr#. Abyssal and fore-arc peridotite fields after Tamura & Arai (2006). (e) Spinel Cr# vs. $Fe^{+3}/\Sigma Fe$.

relative to the MREE and HREE (La/Sm 0.3–0.5, La/Yb 0.6–1.1, Supplemental Data Figure S2).

Plagioclase: Moffett plagioclase are consistently anorthite-rich (An_{91}-An_{93}) and unzoned. Plagioclase from amphibole gabbro MM-76-4 shows similar trace element chemistry to those from Adagdak, with enrichment in the LILE and LREE but depletion in HREE and HFSE. All analyses from this sample show positive Ba, Pb, Sr, and Eu anomalies on primitive mantle normalized trace element diagrams (Supplemental Data Figure S3).

Spinel: Magnetite is the dominant oxide phase in the Moffett cumulates. Chromium-rich spinel is only present in olivine clinopyroxenites MOF-81X-A, MM-CB-2, and MM-77-67, with core Cr# ranging from 73.5 to 82.3 (Fig. 5d). Average calculated $Fe^{3+}/\Sigma Fe$ ranges from 0.25 to 0.42 for spinel cores and does not correlate with Mg# or Cr# (Fig. 5e). The Wood and Virgo correction was not applied to these analyses because the Moffett spinels are far more chromium-rich than any of the secondary spinel standards we measured (Cr# 4–57: Supplemental Data Table S7; Wood & Virgo, 1989; Bryndzia & Wood, 1990).

DISCUSSION

In the following sections, we use our data to investigate the petrogenesis of the cumulate xenoliths and the magmatic plumbing system beneath Adak. We first use our petrographic and major and trace element data to estimate the crystallization sequence, P–T–H_2O–fO_2, and parental melt trace element compositions for the cumulates. We then construct a series of trace element models to explore the petrogenesis of the parental melts to the cumulates and how these melts may have evolved through lower to mid-crustal fractionation of our cumulate lithologies.

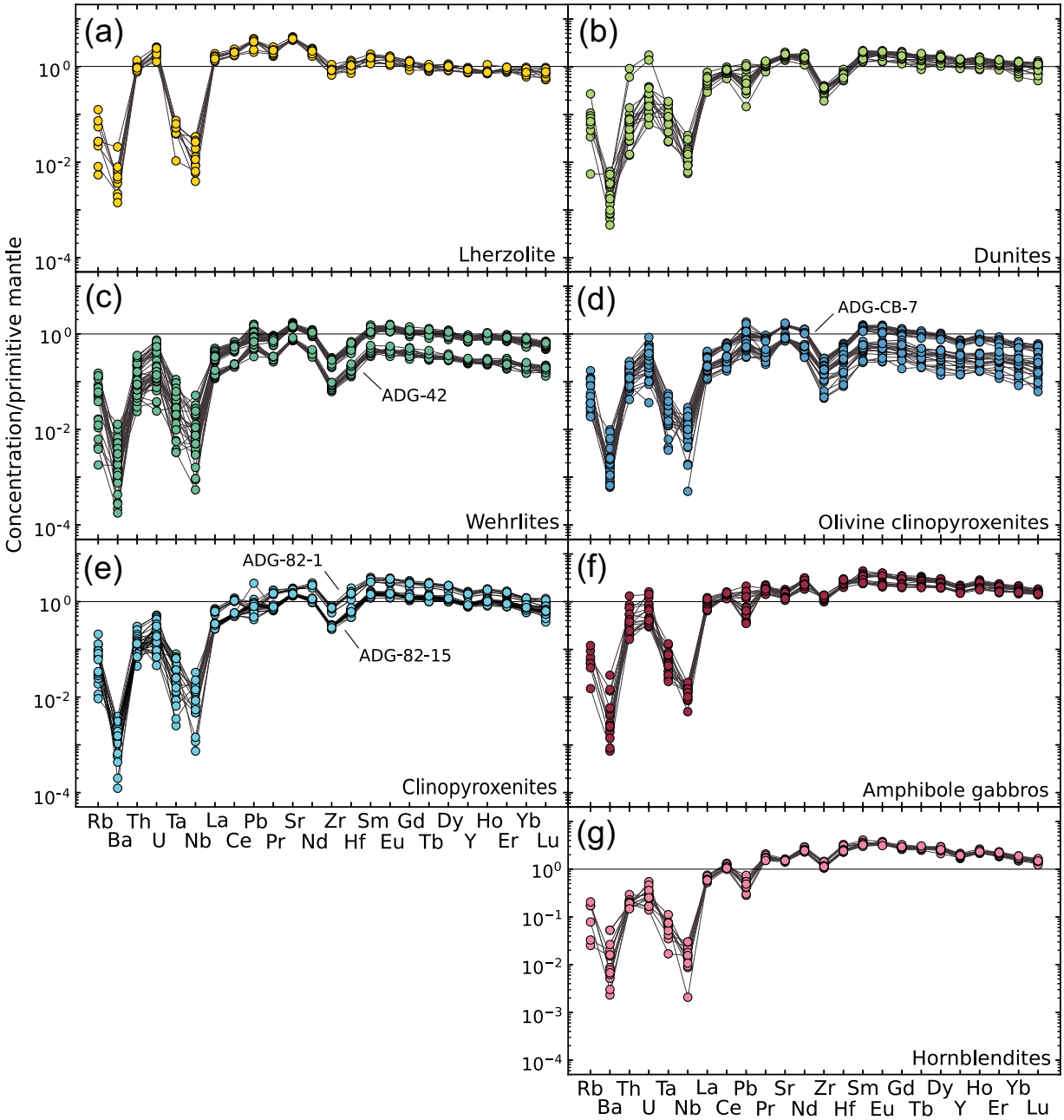

Fig. 6. Primitive mantle normalized trace element concentrations in Adagdak xenolith clinopyroxenes. (a) Amphibole gabbros. (b) Hornblendites. (c) Clinopyroxenites. (d) Olivine clinopyroxenites. (e) Wehrlites. (f) Dunites. (g) Lherzolite.

Crystallization sequence

Determining the crystallization sequences of the Moffett and Adagdak cumulate suites is critical to understanding their petrogenesis, as it is controlled in part by the P–T–H_2O–fO_2 conditions of their parental magmas. Although both cumulate suites show evidence for some subsolidus Fe–Mg exchange, we infer the same crystallization sequence for both suites based on olivine, clinopyroxenes, and amphibole Mg#, spinel Cr#, and modal mineralogy (Fig. 9) that were inferred in earlier studies. Both sequences were constructed under the assumption that the most primitive samples should contain the most magnesian-rich silicates, Cr-rich oxides, and the highest modal abundances of olivine. Petrographic examination indicates that when present, olivine and spinel were the first phases to crystallize, then joined by clinopyroxene.

Adagdak

The dunites represent the initial crystallization products of the Adagdak suite. These samples have the highest modal abundances of olivine (93–94%) and the most Mg-rich olivine (Mg# ~87) and clinopyroxene (Mg# 90–91). The modal abundance of olivine decreases as clinopyroxene becomes the dominant phase in the cumulates, as represented by the wehrlite and clinopyroxenite xenoliths. Amphibole and plagioclase then join the cumulate assemblage together as abundances of cumulus clinopyroxene and olivine decrease abruptly (Fig. 2). Magnetite also replaces spinel as the dominant oxide phase. This final stage of the crystallization sequence is represented by the amphibole gabbro and hornblendite cumulates. Although trace amounts of olivine are only present in about half of these samples, clinopyroxene

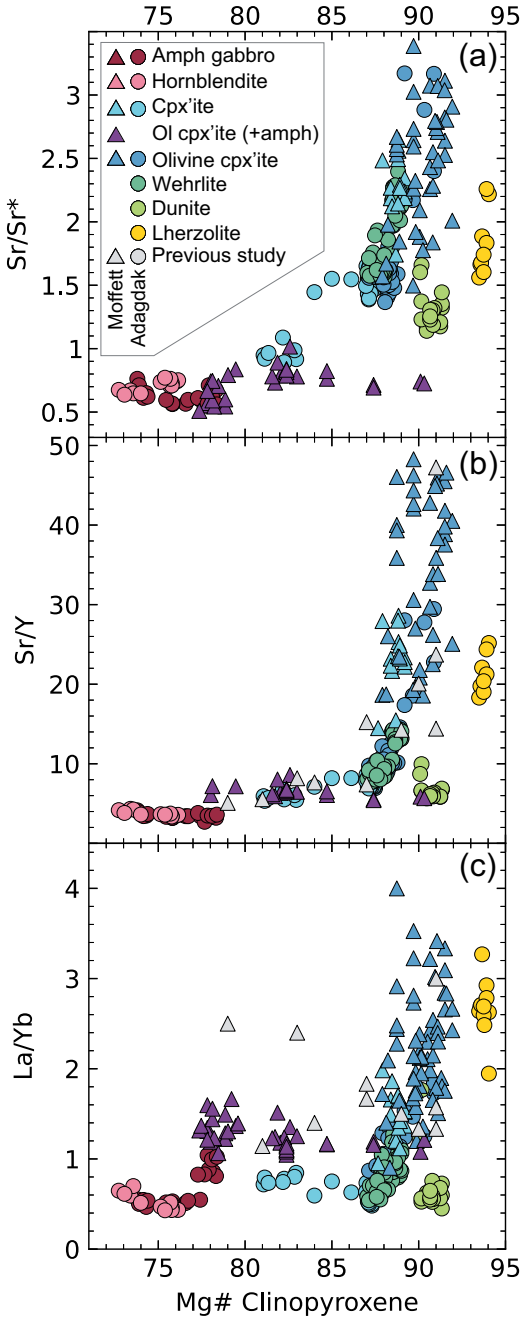

Fig. 7. Clinopyroxene trace element ratios vs. Mg#. (a) Sr/Sr∗ vs Mg#. (b) Sr/Y vs. Mg#. (c) La/Yb vs. Mg#.

persists to the end of the observed sequence. While the amphibole veins observed in some of the ultramafic samples are interpreted to be peritectic in origin, amphibole in all but four of the hornblendites and amphibole gabbros is inferred to be a primary cumulate phase (consistent with the interpretation of Debari *et al.*, 1987). This interpretation is supported petrographically, with amphiboles in these more evolved cumulates usually present as large euhedral grains in no apparent reaction relationship with clinopyroxene or olivine (Fig. 4c). Amphibole in samples ADG-4, -38, -73, and -82–6 is texturally distinct, poikilitically enclosing rounded clinopyroxene (Fig. 4d). This texture could be interpreted two ways: (1) late-stage cumulate amphibole fractionation, with amphibole enveloping pre-existing clinopyroxene grains, or (2) amphibole forming through peritectic reactions between melts percolating through the cumulate mush and preexisting clinopyroxenes (e.g. Cooper *et al.*, 2016; Blatter *et al.*, 2017). The petrography suggests, however, that the vast majority of amphibole in the Adagdak amphibole gabbros and hornblendites co-crystallized with clinopyroxene without evidence for a peritectic relationship. Thus, the dominant inferred crystallization sequence for the Adagdak xenolith suite is olivine + clinopyroxene + spinel ➔ clinopyroxene + amphibole + plagioclase + Fe–Ti oxide.

Moffett

The most primitive crystallization assemblages in the Moffett suite are olivine clinopyroxenites with minor Cr-spinel. Half of these samples also contain amphibole. While the altered appearance of amphibole in MOF-81X-G suggests a secondary or peritectic origin, the petrography of amphiboles in samples MM-77-35 and MM-77-67 is consistent with amphibole being a primary cumulate phase (Fig. 4e, additional photos in the Supplemental Data). The co-crystallization of high-magnesium amphibole, clinopyroxene, and olivine is consistent with derivation from a hydrous primitive basalt or basaltic andesite (Conrad & Kay, 1984; Krawczynski *et al.*, 2012). Conrad & Kay (1984) came to a similar conclusion, suggesting (based on high Cr concentrations in amphiboles from Moffett xenolith MM-102) that amphibole was a near-liquidus phase. Plagioclase subsequently enters the crystallization assemblage while amphibole and magnetite modal abundances increase, as observed in the amphibole gabbro and hornblendite xenoliths. The onset of plagioclase crystallization coincides with a decrease in clinopyroxene abundances (21 to 0%; Fig. 3) and the loss of olivine from the cumulate assemblage. The inferred crystallization assemblage for the Moffett cumulates, as also suggested by Conrad & Kay (1984), is olivine + clinopyroxene + spinel ➔ olivine + clinopyroxene + spinel + amphibole ➔ clinopyroxene + amphibole + plagioclase + Fe–Ti oxide ➔ amphibole + plagioclase + Fe–Ti oxide.

Crystallization conditions

We estimate crystallization conditions (H_2O, P, T, fO_2) through (1) comparison with experimental studies where these variables are controlled, (2) comparison to xenoliths from other localities where crystallization conditions have been inferred or calculated, and (3) calculation of temperature and fO_2 where geothermometers and oxybarometers suitable to the xenolith mineral assemblages are available.

Water contents

Adagdak: Crystallization assemblages from the experimental studies of Nandedkar *et al.* (2014) (N14) and Ulmer *et al.* (2018) (U18) resemble the Adagdak xenolith assemblages. These studies performed equilibrium and fractional crystallization experiments on primitive basalts (Mg# 69.0–76.4) at 0.7–1 GPa, 0 to 2 log units above the Ni–NiO buffer, and hydrous (~3 wt % H_2O initial) conditions. The crystallization sequence, modal proportions, and mineral chemistry of crystallization assemblages produced in these experiments are summarized in the Supplemental Data. The ultramafic cumulates from Adagdak likely crystallized from a primitive basalt with a similar water content to that of the high temperature (1200–1060°C) initial crystallization interval of basalt in U18 and N14 (3–7 wt % H_2O). Characteristics of the Adagdak suite such as the modal dominance of olivine in the early crystallizing assemblages, and the late appearance of plagioclase, are also consistent with derivation from a hydrous melt (Nicholls & Ringwood, 1973; Gaetani *et al.*, 1993;

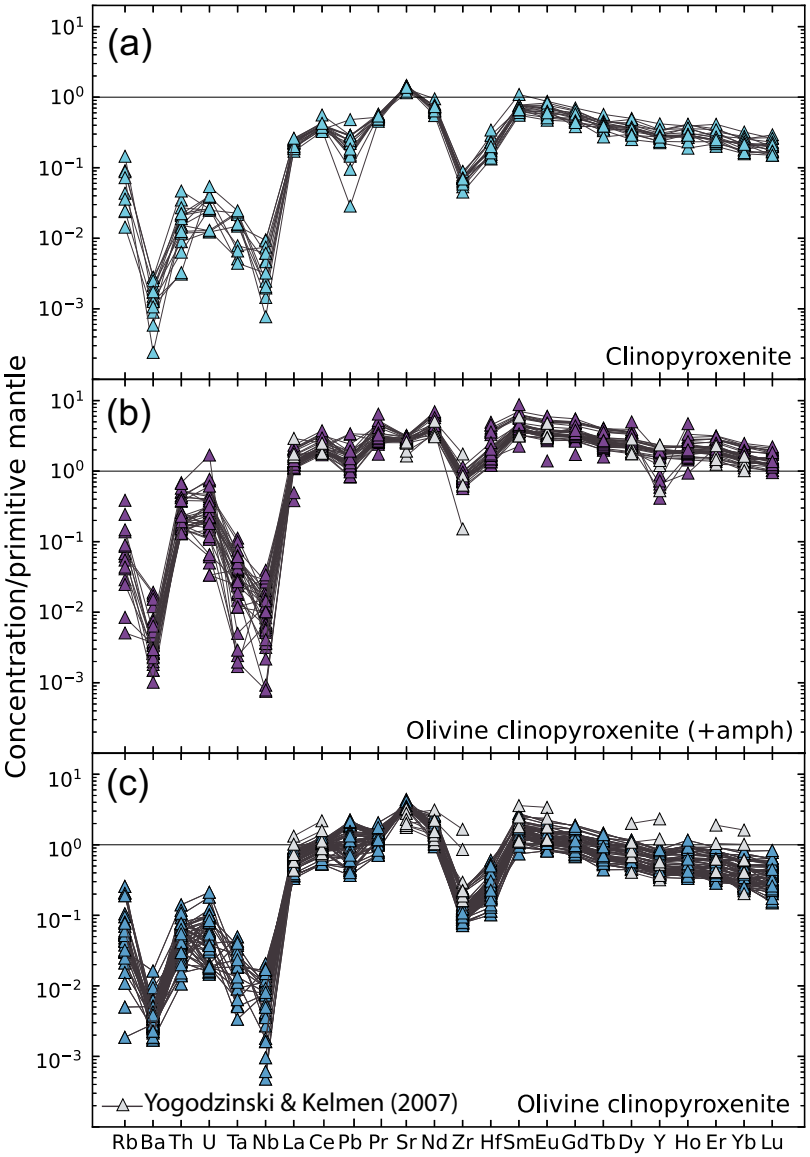

Fig. 8. Primitive mantle normalized trace element concentrations in Moffett xenolith clinopyroxene. (a) Clinopyroxenites. (b) Amphibole-bearing olivine clinopyroxenites. (c) Olivine clinopyroxenites.

Pichavant & Macdonald, 2007; Ulmer *et al.*, 2018). The modal mineralogy and mineral chemistry of the Adagdak amphibole gabbros and hornblendites are similar to lower-temperature (920–730°C) experimental assemblages of N14 which contained 8 to 12 wt % H_2O. We suggest that during the crystallization of the Adagdak suite, early olivine, spinel, and clinopyroxene crystallization from a relatively hydrous basalt (3–7 wt % H_2O) produced the dunites, wehrlites, and clinopyroxenites. Fractionation of these nominally anhydrous phases increased the water content of later-stage melts to 8 to 12 wt % H_2O, at which point the amphibole gabbro and hornblendite cumulates crystallized.

Moffett: The presence of amphibole in the Moffett ultramafic olivine clinopyroxenites and the absence of early plagioclase suggests that the parental melt to the suite had higher water contents than parental melts to the Adagdak suite. The experiments of Krawczynski *et al.* (2012) (K12) on basaltic starting materials provide a close experimental comparison to the ultramafic Moffett crystallization assemblage of olivine, clinopyroxene, and (±) amphibole. These experiments show that water-saturated basalts may simultaneously stabilize olivine, clinopyroxene, and amphibole at 500–800 MPa and water-saturated conditions after about 30% solidification and at <1000°C. Plagioclase-free assemblages of clinopyroxene and amphibole (±olivine and spinel) have also been produced in crystallization experiments of hydrous (>7 wt % H_2O) basalts by Melekhova *et al.* (2015) and Ulmer *et al.* (2018). The phase assemblage and mineral chemistry of Moffett amphibole gabbros and hornblendites are very similar to those from Adagdak. We, therefore, estimate that the parental melts to the Moffett amphibole gabbro and hornblendite cumulates were also saturated with an H_2O-rich fluid in the lower to middle crust.

Pressure

As is common for garnet-free ultramafic and mafic igneous assemblages, the mineralogy of the Adak xenoliths does not lend itself well to thermodynamically based geobarometry (Debari *et al.*, 1987; Bryndzia & Wood, 1990; Wood *et al.*, 1990;

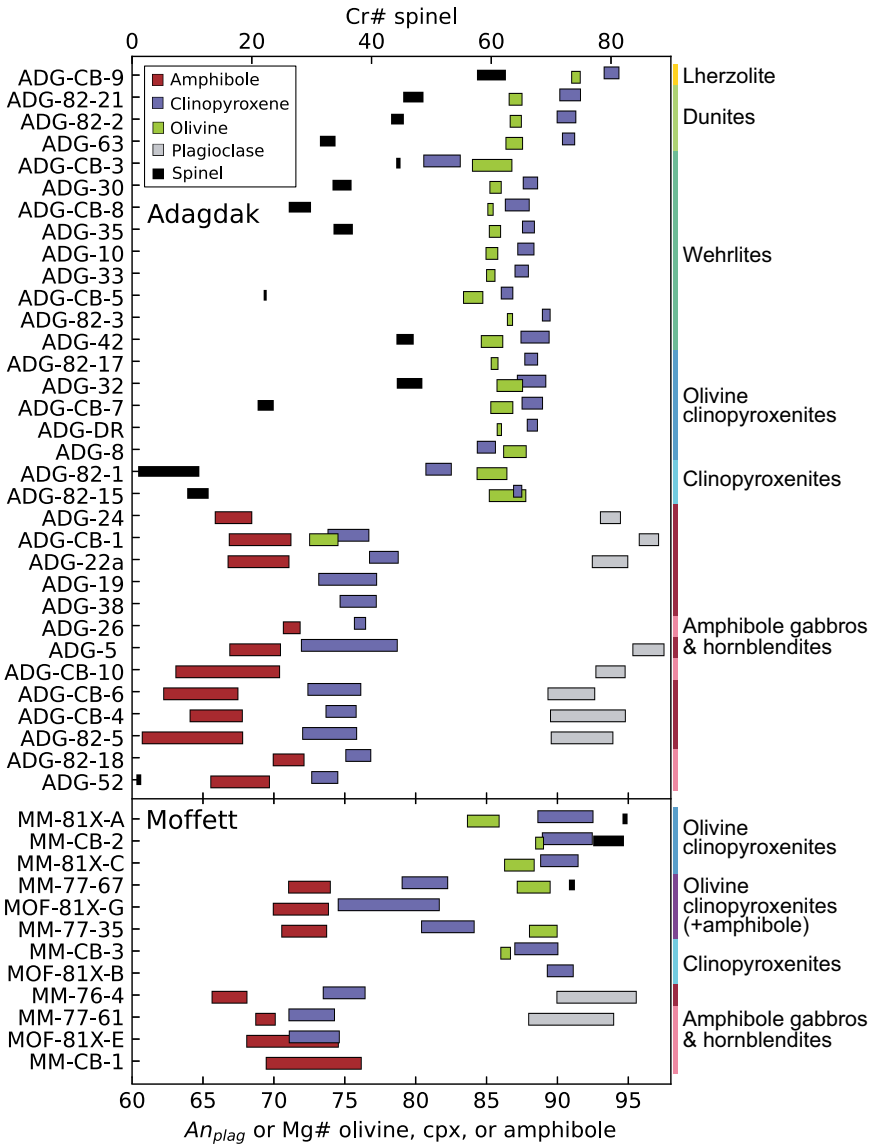

Fig. 9. Summary of major element mineral chemistry for the Adagdak and Moffett xenoliths suites. Samples are ordered by modal abundance of olivine.

Davis *et al.*, 2017; Bucholz & Kelemen, 2019). We, therefore, derive pressure estimates by comparing our samples to experimental studies where pressure was controlled as well as to xenoliths from other locations where pressure is well constrained.

Adagdak: We infer that the Adagdak ultramafic cumulates crystalized at ~1 GPa. This estimate is consistent with experimental studies that have produced assemblages modally and geochemically similar to the Adak cumulates (Blatter *et al.*, 2013; Ulmer *et al.*, 2018) as well as previous studies of Adak and central Aleutian magmatism that place crystallization of the most primitive lithologies at the base of the arc crust (Gust & Perfit, 1987; Kay & Kay, 1994; Kay *et al.*, 2019). Our ~1 GPa estimate is also consistent with previous studies of Aleutian magmas, which have suggested that plagioclase-free ultramafic cumulate fractionation in the upper mantle and lower crust leads to the formation of the high-Al basalts found on Adak Island and throughout the Aleutians (Kay & Kay, 1985a, 1985b). The high-Mg basalt crystallization experiments from U18 that we use as our primary experimental comparison for these most primitive Adagdak cumulates were also conducted at 1 GPa.

The negative correlation between clinopyroxene Mg# and Al_2O_3 observed in the ultramafic cumulates (Fig. 5c) is also consistent with plagioclase-free crystallization under high-pressure or high-water conditions (DeBari *et al.*, 1987; DeBari & Coleman, 1989; Melekhova *et al.*, 2015). Similar trends are seen in clinopyroxenes from intermediate to high-pressure exhumed arc sections (e.g. the Chilas Complex, Kohistan, 0.5–0.8 GPa: Jagoutz *et al.*, 2007; Talkeetna, 0.95–1.1 GPa: DeBari & Coleman, 1989), but are not observed in clinopyroxenes from low-pressure cumulates (e.g. Lesser Antilles, 0.2–0.5 GPa: Stamper *et al.*, 2014a; Cooper *et al.*, 2016). Due to the expanded stability field of clinopyroxene at higher pressures (e.g. Blatter *et al.*, 2013; Stamper *et al.*, 2014b), early fractionation of clinopyroxene + olivine assemblages also results in the Adagdak wehrlites containing more magnesian olivine (Mg# 84.1 to 86.7) than is observed in wehrlites from lower pressure systems (e.g. Lesser Antilles, wehrlite olivine Mg# = 82.5 ± 2, Stamper *et al.*, 2014a)

Due to the similarities discussed previously between 0.7 GPa experiments from N14 and the Adagdak amphibole gabbro and hornblendite cumulates, it is tempting to assert that this pressure

Table 3: Calculated temperature, silica activity, and oxygen fugacity estimates

Sample	Pressure (kbar)		Temperature estimates (°C)					
	Amphibole-only		*Fe–Mg exchange*				*Ca-in-olivine*	
	R2021		*L1995*		*B1991*		*S&C2013*	
	Ave.	**2σ[a]**	**Ave.**	**2σ[b]**	**Ave.**	**2σ[b]**	**Ave.**	**2σ[c]**
ADG-82-5	4.77	±0.79						
ADG-CB-4	7.48	±1.89						
ADG-26	6.20	±0.56						
ADG-CB-6	3.94	±0.81						
ADG-5	5.88	±0.73						
ADG-CB-10	6.6	±1.97						
ADG-82-18	9.08	±0.66						
ADG-22a	4.79	±1.24						
ADG-24	4.65	±0.34						
ADG-52	6.41	±0.88						
ADG-CB-1	4.93	±0.78						
ADG-82-15			914	+42/−49	886	±50		
ADG-CB-7			1173	+40/−39	1127	±20	947	+21/−25
ADG-32			1029	+20/−27	1069	±23	965	+23/−10
ADG-82-17							935	+9/−4
ADG-42			1066	+38/−24	1133	±22	946	+19/−20
ADG-CB-5							943	+6/−8
ADG-35			1026	+25/−17	1113	±18	961	±6
ADG-30			1057	+35/−20	1053	±25	968	+12/−29
ADG-CB-3			998	+5/−11	1106	±4	1001	+7/−8
ADG-82-21			1106	+34/−35	1146	±31	923	+13/−15
ADG-63			1049	+28/−22	1060	±17	930	+42/−53
ADG-82-2			1051	+35/−25	1087	±14	990	+46/−52
ADG-CB-9			1080	+27/−23	1101	±25	942	+17/−45
MM-CB-1	6.38	±1.7						
MOF-81X-E	7.33	±1.85						
MM-77-61	6.79	±0.41						
MM-76-4	7.40	±2.65						
MM-77-35	3.90	±0.25					1107	+17/−50
MOF-81X-C							1044	+16/−30
MM-77-67	6.65	±0.38					1106	+8/−35

regime is also an appropriate estimate for these lithological groups. However, because amphibole–plagioclase-magnetite assemblages are ubiquitous in rocks from various crustal depths (e.g. Lesser Antilles, 0.2–0.5 GPa: Cooper *et al.*, 2016; Kohistan, 0.5–0.8 GPa: Jagoutz *et al.*, 2007; Talkeetna, 0.95–1.1 GPa: DeBari & Coleman, 1989) comparisons based on similarities in phase proportions are not as useful. Due to the lack of thermodynamically based geobarometers available, we also implement empirical amphibole-only geobarometry for both Adagdak and Moffett cumulates. Empirical amphibole-only geobarometry (Ridolfi, 2021) yields pressure estimates between 390 and 910 MPa for the Adagdak amphibole gabbros and hornblendites, consistent with mid- to deep crustal pressures and the large range of pressures over which amphibole gabbros can crystallize (Table 3).

Moffett: The ultramafic olivine + clinopyroxene ± amphibole/Fe–Ti oxide Moffett assemblage has been produced by experimental studies over a pressure interval of 0.2 to 0.8 GPa (Holloway & Burnham, 1972; Cawthorn *et al.*, 1973; Helz, 1973; Sisson & Grove, 1993; Krawczynski *et al.*, 2012). The amphibole-only geobarometer of Ridolfi (2021) yields pressure estimates of 0.4 to 0.7 GPa for these lithologies, within this range (Table 3). For the amphibole gabbros and hornblendites, amphibole-only geobarometry yields pressures between 0.6 and 0.7 GPa (Ridolfi, 2021) (Table 3). In summary, the mineral chemistry and phase assemblages observed in the Moffett cumulate suite are generally consistent with crystallization in the lower to middle crust, between 0.4 and 0.7 GPa.

Temperature

For ultramafic xenoliths containing the assemblage olivine + clinopyroxene + spinel, we used the olivine-spinel Fe–Mg exchange thermometers of Ballhaus *et al.* (1991) and Li *et al.* (1995) (n = 11). For the 15 samples from which we obtained high-precision analyses of the Ca content of olivine, we also calculated temperature with the Ca-in-olivine thermometers of Shejwalkar & Coogan (2013) and Köhler & Brey (1990). The empirical amphibole-only thermometer of Ridolfi (2021) was used to obtain temperature estimates for amphibole gabbros and hornblendites (n = 17). For xenoliths, for which we had both amphibole and plagioclase mineral chemistry, we used the amphibole–plagioclase thermometer of Holland & Blundy (1994) to estimate temperature (n = 10). The results of these calculations are given in Table 3.

Adagdak: For the lherzolite, both olivine-spinel Fe–Mg exchange thermometers yield temperatures that are within error of each other, ranging from 1080°C to 1100°C. For the ultramafic cumulate xenoliths (n = 11), Fe–Mg exchange temperatures obtained with

Table 3: continued

Sample	Temperature estimates (°C)					
	Ca-in-olivine		*Amphibole-only*		*Amphibole–plagioclase*	
	K&B1990		*R2021*		*H&B1994*	
	Ave.	**2σ [c]**	**Ave.**	**2σ [d]**	**Ave.**	**2σ [e]**
ADG-82-5			925	±13	1022	+21/−31
ADG-CB-4			964	±15	996	+22/−23
ADG-26			933	±9		
ADG-CB-6			923	±12	1049	+22/−28
ADG-5			939	±12	917	+52/−43
ADG-CB-10			953	±18	1014	±31
ADG-82-18			968	±24		
ADG-22a			931	±23	1063	+44/−43
ADG-24			929	±12	1074	±23
ADG-52			927	±15		
ADG-CB-1			919	±9	1039	+27/−23
ADG-82-15						
ADG-CB-7	971	+24/−2				
ADG-32	991	+16/−17				
ADG-82-17	971	±4				
ADG-42	997	+11/−31				
ADG-CB-5	993	+48/−7				
ADG-35	978	-20/+23				
ADG-30	977	±4				
ADG-CB-3	1040	±8				
ADG-82-21	961	+19/−22				
ADG-63	1012	+23/−26				
ADG-82-2	944	+15/−26				
ADG-CB-9	936	+15/−16				
MM-CB-1			940	±20		
MOF-81X-E			954	±25		
MM-77-61			951	±11	895	+34/−35
MM-76-4			959	±38	921	+29/−30
MM-77-35	1107	+35/−43	917	±8		
MOF-81X-C	1070	+23/−27				
MM-77-67	1104	+21/−23	963	±16		

the Ballhaus *et al.* (1991) and Li *et al.* (1995) thermometers are generally within error of each other (Supplemental Data Figure S4), ranging from 1000°C to 1150°C. Temperature estimates were also obtained with the olivine-clinopyroxene calcium exchange thermobarometers of Shejwalkar & Coogan (2013) (their equation 13) and Köhler & Brey (1990) (their equation 5). Both thermobarometers are calibrated on experiments ranging from 0.1 to 6 GPa and both were evaluated at 1 GPa. Temperature estimates obtained with Ca-in-olivine thermometry range from 920°C to 1040°C for the ultramafic cumulates (n = 12) and were generally 40°C to 230°C lower than temperature estimates obtained through Fe–Mg exchange thermometry. The low Ca-in-olivine temperature estimates may reflect subsolidus diffusion of Ca from olivine (Dohmen *et al.*, 2017) or variations in the calcium activity coefficient in forsterite and monticellite activity with changing bulk composition or pressure (Shejwalkar & Coogan, 2013).

Taken together, the temperatures these samples preserve (950–1150°C) are consistent with experimental studies of hydrous basalts that produced similar assemblages of olivine + clinopyroxene + spinel (1050–1200°C, Pichavant & Macdonald, 2007; Nandedkar *et al.*, 2014; Ulmer *et al.*, 2018) and suggests Fe–Mg exchange thermometry broadly preserves magmatic crystallization temperatures. Amphibole-only thermometry for the amphibole gabbros and hornblendites yields temperatures from 920°C to 970°C (n = 11). Amphibole–plagioclase thermometry (n = 8; Holland & Blundy, 1994) yields temperatures between 920°C and 1070°C. Amphibole–plagioclase temperatures are generally 60°C to 140°C higher than those obtained with amphibole-only thermometry.

Moffett: The Moffett cumulates broadly preserve crystallization temperatures between 900°C and 1100°C. Fe–Mg olivine-spinel exchange thermometry in ultramafic samples MM-77-67, MOF-81X-A, and MM-CB-2) yielded temperatures of 855–2/+4, 1045 ± 3, and 1140 + 10/−17°C. We consider 860°C and 1140°C to be erroneous estimates, as they are inconsistent with experimental studies that have crystalized olivine + clinopyroxene + amphibole assemblages over a limited temperature range (900–1050°C; Holloway & Burnham, 1972; Cawthorn *et al.*, 1973; Helz, 1973; Krawczynski *et al.*, 2012). Low olivine-spinel temperatures may be due to subsolidus Fe–Mg exchange in the Moffett samples, as evidenced by the large variations in $K_{Ol-CPX}^{Fe^T/Mg}$ observed in the Moffett suite (Fig. 5b), or re-equilibration of small chromite grains with the surrounding olivine (e.g. Peltonen, 1995). Moffett Ca-in-olivine thermometry (n = 3) was conducted at 0.7 GPa (based on the discussion in the previous section) and yielded temperature estimates between 1040°C and 1105°C. Amphibole-only thermometry ranged from 920°C to 960°C (Supplemental Data Figure S4). Amphibole–plagioclase thermometry for samples

Table 3: continued

Sample	Silica activity estimates			Oxygen fugacity estimates								
	log(aSiO $_2$)			**method A**			**method B**			**method C**		
	B&K2019			*B&K2019*			*B1991*			*D2017*		
	Ave	$2\sigma^f$	ΔEn-Fo	log(fO_2)	$2\sigma^f$	ΔFMQ	log(fO_2)	$2\sigma^f$	ΔFMQ	log(fO_2)	$2\sigma^f$	ΔFMQ
ADG-82-15							−10.15	+0.47/−1.00	1.32			
ADG-CB-7	−0.406	+0.05/−0.11	−0.010	−6.09	+0.42/−0.55	1.76	−6.66	+0.33/−0.52	1.19			
ADG-32	−0.476	+0.15/−0.5	−0.018	−9.09	+0.29/−0.49	0.60	−7.96	+0.27/−0.37	1.73			
ADG-42	−0.441	+0.09/−0.08	0.001	−8.17	+0.63/−0.39	1.02	−7.48	+0.47/−0.32	1.71			
ADG-35	−0.471	±0.03	−0.011	−9.13	+0.46/−0.31	0.61	−8.24	+0.40/−0.16	1.49			
ADG-30	−0.456	+0.05/−0.04	−0.011	−8.54	+0.55/−0.38	0.77	−7.85	+0.44/−0.26	1.46			
ADG-CB-3	−0.521	±0.03	−0.042	−10.10	+0.21/−0.40	0.10	−8.06	+0.05/−0.23	2.14			
ADG-82-21	−0.404	+0.06/−0.05	0.019	−7.15	+0.50/−0.56	1.51	−7.19	+0.41/+0.44	1.48			
ADG-63	−0.444	+0.21/−0.16	0.005	−8.29	+0.39/−0.36	1.13	−7.98	+0.35/−0.28	1.44			
ADG-82-2	−0.431	+0.03/−0.15	0.017	−8.79	+0.54/−0.41	0.60	−7.78	+0.45/−0.33	1.61			
ADG-CB-9	−0.388	+0.15/−0.11	0.047	−7.84	+0.35/−0.56	1.16	−7.71	+0.34/−0.30	1.30	−8.05	+0.43/−0.25	1.02

R2021 Ridolfi, 2021; *L1995* Li *et al.* (1995); *B1991* Ballhaus *et al.* (1991); *S&C2013* Shejwalkar & Coogan (2013); *K&B1990* Köhler & Brey (1990); *B&K2019* Bucholz & Kelemen (2019); *D2017* Davis *et al.* (2017)

[a]Pressure estimates were obtained for each amphibole core analysis. Uncertainties represent 2 standard deviations the range for those calculated pressures per sample.

[b]Uncertainties calculated using average olivine compositions and calculating a different temperature for each core spinel analysis (15–50 per sample).

[c]Uncertainties calculated by varying X_{Mo} to the minimum and maximum values obtained for each sample (for S&C2013, X_{Fo} was fixed to its average value)

[d]Temperature was calculated for each amphibole analysis. Uncertainties represent 2 standard deviations the range for those calculated temperatures per sample.

[e]Uncertainties calculated by fixing the plagioclase composition and calculating a different temperature for each amphibole analysis.

[f]Uncertainties calculated by varying temperatures obtained through olivine-spinel thermometry (L1995) to their maximum and minimum values.

MM-77-61 and MM-76-4 yields respective temperatures of 900°C and 920°C.

Oxygen fugacity

Adagdak: Thermodynamic oxybarometers for mantle rocks typically rely on phase equilibria between the fayalite component of olivine, the ferrosilite component of orthopyroxene, and the magnetite component of spinel. The ferrosilite component of orthopyroxene is employed to estimate silica activity in the redox reaction between fayalite and magnetite (Mathez, 1984; Mattioli & Wood, 1988; Wood & Virgo, 1989; Ballhaus *et al.*, 1991). Because our Adagdak cumulates do not contain orthopyroxene, we estimated silica activity using diopside-monticellite equilibria following the methods of Bucholz & Kelemen (2019). High-precision Ca-in-olivine analyses were used to determine the monticellite component of olivine (X_{Mo}) for these calculations, obtaining fO_2 values 0.1 to 1.8 log units above the fayalite-magnetite-quartz (FMQ) buffer for the cumulates (n = 9) and a value of FMQ +1.2 for lherzolite ADG-CB-9 (method A in Table 3, Supplemental Data Figure S5).

Using the oxybarometer of Ballhaus *et al.* (1991), we calculate fO_2 values from FMQ +1.2 to +2.1 for the Adagdak cumulates and FMQ +1.3 for the lherzolite (method B in Table 3). This oxybarometer can be implemented on samples with only spinel and olivine present; however, the reduced silica activity in these systems can lead to overestimates of fO_2 up to +0.6 log units. For samples lacking orthopyroxene (i.e. all but ADG-CB-9), these estimates must, therefore, be taken as upper fO_2 limits. For the lherzolite, we also calculated fO_2 with olivine–orthopyroxene–spinel oxybarometry using the parameterization of Davis *et al.* (2017), yielding a value of FMQ +1.02 + 0.43/−0.25.

These are the second direct estimates of fO_2 for oceanic arc lower crustal cumulates through olivine–spinel oxybarometry. Consistent with a previous study of Talkeetna arc cumulates (FMQ +0.4 to +2.3: Bucholz & Kelemen, 2019), our fO_2 estimates (FMQ +0.1 to +2.1) support other studies indicating that the lower crust and upper mantle of oceanic arcs are oxidized relative to MORB (ΔFMQ = 0.16 ± 0.01; Cottrell & Kelley, 2011). These values are consistent with studies of sub-arc mantle xenoliths (FMQ +0.5 to +2.9: Parkinson & Pearce, 1998; Parkinson & Arculus, 1999; Parkinson *et al.*, 2003; Bryant *et al.*, 2007; Ichiyama *et al.*, 2016) and arc lavas, which studies consistently show to be oxidized relative to MORB (FMQ + 0.5 to +3.5; Kelley & Cottrell, 2009; Brounce *et al.*, 2014; Richards, 2015; Cottrell *et al.*, 2021).

While the mineral assemblage in the amphibole gabbros and hornblendites (clinopyroxene + amphibole + plagioclase + magnetite) does not allow us to rigorously interrogate their fO_2s through phase equilibria, the high amphibole/clinopyroxene ratios in these samples and the shift in oxide compositions from spinel to magnetite is consistent with fractionation from an oxidized melt. Ulmer *et al.* (2018) found in their equilibrium crystallization experiments of high-Mg basalts that as the melt fraction decreased in lower temperature runs, the fO_2 of the remaining liquid in the charges increased from ~FMQ +2 to +6. They attributed this apparent auto-oxidation of the system to the removal of Fe^{2+} from the melt by olivine and clinopyroxene fractionation, increasing the $Fe^{3+}/\Sigma Fe$ ratio of the remaining late-stage melts. A similar scenario may be envisioned for Adagdak, in which olivine and clinopyroxene fractionation leads to auto-oxidation of the melt, increasing fO_2 in the late-stage magmas that crystalized the amphibole gabbro and hornblendite cumulates (e.g. Kelley & Cottrell, 2012).

Moffett: Due to the paucity of spinel in Moffett xenoliths, we cannot confidently estimate fO_2 for the Moffett cumulates. Taking our Fe–Mg exchange temperature estimates and mineral chemistry for spinel-bearing samples MM-CB-2, MM-77-67, and MOF-81X-A, and applying the Ballhaus *et al.* (1991) oxybarometer at 0.7 GPa yields fO_2 estimates between FMQ +1.4 and +2.1. Although the lack of satisfactory temperature constraints renders these values approximations, they are broadly consistent with

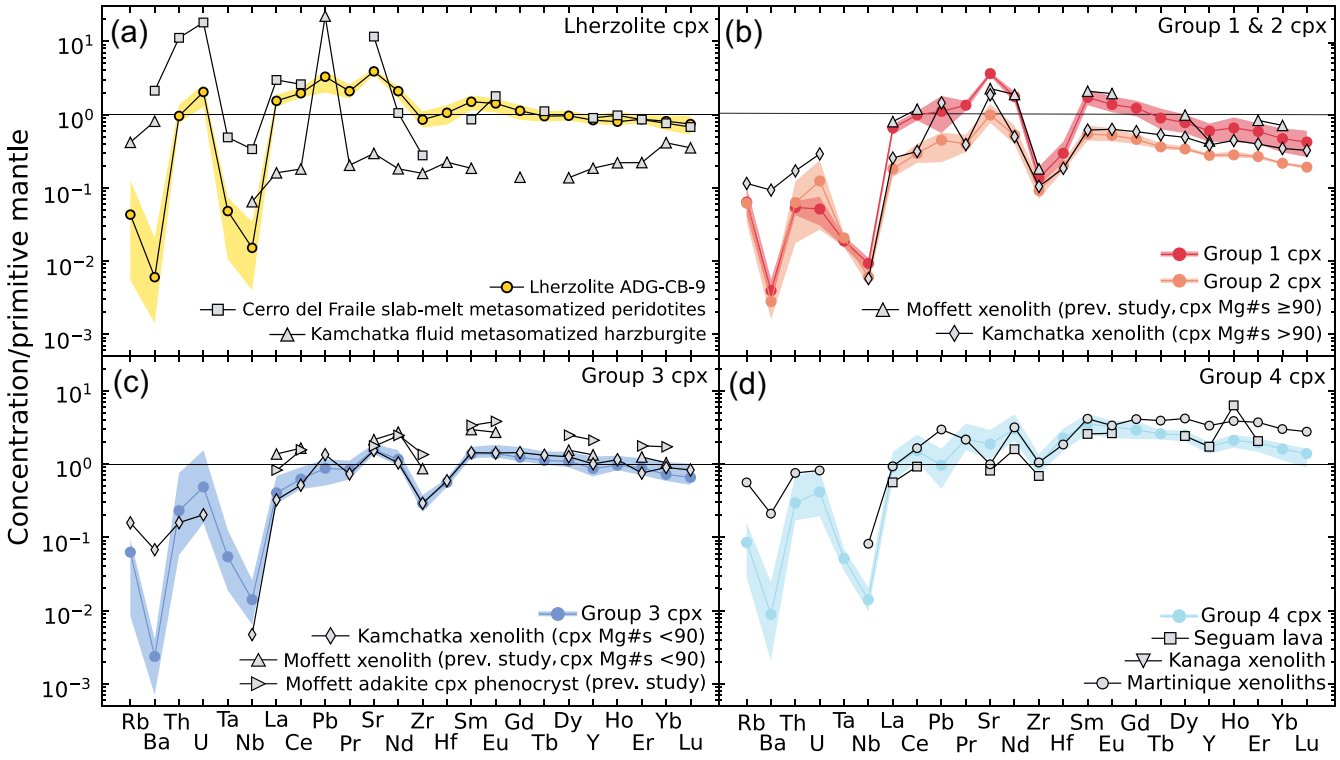

Fig. 10. Clinopyroxene trace element concentrations organized by compositional groups. Solid lines and shaded regions represent the averages and variability observed in samples or compositional groups, respectively. (a) Lherzolite ADG-CB-9 clinopyroxene. Trace element data from (1) slab-melt metasomatized mantle xenolith clinopyroxene, Cerro del Fraile, Southern Patagonia (Kilian & Stern, 2002) and (2) fluid metasomatized mantle xenolith clinopyroxene from Kamachatka (Ishimaru *et al.*, 2006) is also shown. (b) Clinopyroxene compositional Groups 1 and 2. High Mg# (>90) clinopyroxene trace element data from Kamchatka cumulate xenoliths (Siegrist *et al.*, 2019) and a previous study of Moffett cumulates (Yogodzinski & Kelemen, 2007) are shown for comparison. (c) Clinopyroxene compositional Group 3. Low Mg# (<90) clinopyroxene trace element data from the Kamchatka (Siegrist *et al.*, 2019), Moffett cumulates, and cpx phenocrysts from Moffett adakite MM79A (Yogodzinski & Kelemen, 2007) are shown for comparison. (d) Clinopyroxene compositional Group 4. Clinopyroxene trace elements from (1) Kanaga Island (Yogodzinski & Kelemen, 2007) and Martinique Island (Cooper *et al.*, 2016) cumulate xenoliths and (3) Seguam Island basalts (Yogodzinski & Kelemen, 1998) are given for comparison.

comparisons to experimental studies, which also suggest the ultramafic cumulates crystalized under oxidizing conditions. The experimental studies that produced assemblages similar to the Moffett cumulates were all conducted at oxygen fugacities between the NNO and hematite magnetite (HM) redox buffers (FMQ +0.25 to +4.4; Holloway & Burnham, 1972; Helz, 1973; Krawczynski *et al.*, 2012). We, therefore, infer that the Moffett xenoliths suite also crystalized under oxidizing conditions, perhaps more so than the Adagdak suite, although we cannot give precise nor quantitative estimates.

Trace elements

Clinopyroxene trace element groups

For the purposes of discussion, we break our cumulate samples into four compositional groups based on similarities in clinopyroxene trace element chemistry, while the lherzolite is discussed separately. These groupings are based on the degree of LREE-HREE fractionation, HFSE depletion, the presence or absence of a Sr anomaly, and clinopyroxene Mg#. The average compositions of clinopyroxenes from each group are shown in Figure 10, and each sample is categorized in the Supplemental Data (Table S8). We compare our results to clinopyroxene trace element data of cumulate and peridotite xenoliths from other arc settings where trace element signatures have been attributed to interactions between mantle melts/rocks and basaltic eclogite melts.

Adagdak lherzolite: Clinopyroxene from lherzolite ADG-CB-9 shares trace element characteristics with clinopyroxene from the cumulate xenoliths, such as LREE-HREE fractionation (La/Yb 2.7 ± 0.6) and positive Sr-anomalies (Sr/Sr∗ 1.83 ± 0.48). HFSEs behavior is variable, with lower Ta and Nb (≤11 ng/g) but higher concentrations of Zr and Hf (9.5 and 0.3 μg/g, respectively) compared to the most primitive Adagdak and Moffett cumulates (0.9–4.3 and 0.1–0.2 μg/g, respectively). Clinopyroxene from the lherzolite also has higher Th and U concentrations than observed in the cumulate xenoliths.

Clinopyroxenes from mantle xenoliths from Cerro del Fraile (Southern Patagonia) have similar REE patterns to ADG-CB-9 (e.g. La/Yb = 3.9; Kilian & Stern, 2002). While these clinopyroxenes show some discrepancies with ADG-CB-9 clinopyroxenes regarding absolute HFSE and large ion lithophile element (LILE) concentrations, they show the same general pattern of Th, U, and Sr enrichment with Ta, Nb, and Zr depletion (Fig. 10a). The trace element signatures in the Cerro del Fraile xenoliths were attributed to both cryptic and modal metasomatism of mantle peridotite by a basaltic eclogite melt (Kilian & Stern, 2002). Notably, clinopyroxenes from the ADG-CB-9 are compositionally distinct from those found in both fluid metasomatized and unmetasomatized mantle xenoliths from the Honshu arc (Abe *et al.*, 1998; Ichiyama *et al.*, 2016), Avacha, Southern Kamchatka (Ishimaru *et al.*, 2006),

Mexico (Luhr & Aranda-Gómez, 1997; Mukasa *et al.*, 2007), and the Lesser Antilles (Parkinson *et al.*, 2003; Vannucci *et al.*, 2007), which are typically characterized by flat to HREE enriched trace element profiles (La/Yb generally <1).

Group 1: Group 1 clinopyroxenes are characterized by the greatest enrichment in LREE relative to HREE (La/Yb 1.5–2.5), positive

Sr anomalies (Sr/Sr∗ 1.8–2.8), and significant HFSE depletion (1–2 μg/g Zr, ≤ 8 ng/g Hf, Nb, Ta). This group is composed only of the most magnesian clinopyroxenes in the Moffett suite (Mg# 90–91). Clinopyroxenes in the most primitive (Mg# > 90) cumulate xenoliths from Kharchinsky, Central Kamchatka (Siegrist *et al.*, 2019), as well as those from a previous study of Moffett cumulate xenoliths (Yogodzinski & Kelemen, 2007), are similar to Group 1 clinopyroxene with respect to their trace element characteristics (Fig. 10b). Both of these studies evoked a basaltic eclogite melt component in the parental magmas to the cumulate to explain their trace element characteristics. The presence of these signatures in clinopyroxenes from Group 1 xenoliths may also suggest that an end-member component derived from partial melting of a basaltic eclogite source was present in their parental magmas.

Group 2: This group includes Adagdak cumulates ADG-32 and ADG-42, and Moffett sample MM-CB-3. All samples are ultramafic olivine and clinopyroxene-bearing cumulates. Clinopyroxenes in this group share characteristics with compositional Group 1, such as high Mg# (88–89), similar degrees of LREE-HREE fractionation (La/Yb 0.9–1.5), and positive Sr-anomalies (Sr/Sr∗ 1.8–2.3). However, these clinopyroxene consistently exhibit lower absolute concentrations in all trace elements except Rb, Th, U, and Ta (Fig. 10b). We are not aware of any previous study reporting clinopyroxene trace elements compositions this depleted from an arc-derived lava or related cumulate xenolith.

Group 3: Clinopyroxenes in our third group are characterized by more modest HFSE depletion (2.5–4.3 μg/g Zr, ≤ 20 ng/g Na, Ta, Hf), LREE-HREE fractionation (La/Yb 0.6–1.5), and smaller (although still positive) Sr-anomalies (Sr/Sr∗ 1.3–2.2) than are observed in compositional groups 1 and 2. This group contains Adagdak dunites, wehrlites, and (olivine) clinopyroxenites. The trace element profiles of these clinopyroxenes resemble clinopyroxene phenocrysts from Moffett adakite lavas (Yogodzinski & Kelemen, 2007) and the less magnesian clinopyroxenes (Mg# < 90) in cumulate xenoliths from both Kamchatka (Siegrist *et al.*, 2019; Fig. 10c) and the previous study of Moffett xenoliths by Yogodzinski & Kelemen (2007). The less pronounced basaltic eclogite melt signatures in these cumulates could imply that while the same endmember ascribed to groups 1 and 2 may have been present in the parental magmas to Group 3 samples, its characteristics were diluted by mixing, assimilation, or fractionation processes.

Group 4: Clinopyroxene from the most evolved Adagdak xenoliths (clinopyroxene Mg# < 82) and amphibole-bearing Moffett samples fall into this group. These clinopyroxene have lower Mg# (73–82), more subtle LREE-HREE fractionation (La/Yb 0.5–1.3), and significantly less HFSE depletion (8–15 μg/g Zr, 0.5–1 μg/g Hf) compared Groups 1 to 3 (Fig. 10d). Group 4 clinopyroxene display negative Sr-anomalies (0.6–0.9). Similar trace element characteristics are observed in clinopyroxenes from basaltic lavas from Seguam Island (east of Adak: Yogodzinski & Kelemen, 1998), cumulate xenoliths from the basement of Kanaga Island (west of Adak: Yogodzinski & Kelemen, 2007), and from Martinique in the Caribbean (Cooper *et al.*, 2016) (Fig. 10d). The trace element characteristics of clinopyroxene from these studies are attributed to crystallization from of basaltic arc magmas with little to no input from an eclogite melt.

Taken together, our clinopyroxene trace element data suggest the basaltic eclogite melt component or 'adakite' signature was strongest in the most primitive Moffett and Adagdak cumulates and was diluted or overprinted by the time the more evolved lithologies crystallized. These results are consistent with the previous study of Yogodzinski & Kelemen (2007), who observed positive correlations between Mg# and Sr/Y and La/Yb ratios in the Moffett clinopyroxenes. The similarities in clinopyroxene trace element data between lherzolite ADG-CB-9 and the mantle xenoliths from Patagonia and Kamchatka also suggest the contribution of a metasomatic agent with adakite-like trace element signature.

Table 4: Basalt-cpx partition coefficients

Element	Kd	Reference
Rb	0.0035	Klemme *et al.* (2002)
Ba	0.00068	Hart & Dunn (1993)
Th	0.013	Matsui *et al.* (1977)
U	0.017	Matsui *et al.* (1977)
Ta	0.012	Klemme *et al.* (2002)
Nb	0.0077	Hart & Dunn (1993)
La	0.0536	Hart & Dunn (1993)
Ce	0.0858	Hart & Dunn (1993)
Pb	0.0102	Hauri *et al.* (1994)
Pr	0.11	Klemme *et al.* (2002)
Sr	0.1283	Hart & Dunn (1993)
Nd	0.1873	Hart & Dunn (1993)
Zr	0.093	Klemme *et al.* (2002)
Hf	0.170	Klemme *et al.* (2002)
Sm	0.291	Hart & Dunn (1993)
Eu	0.27	Paster *et al.* (1974)
Gd	0.41	Paster *et al.* (1974)
Tb	0.42	Paster *et al.* (1974)
Dy	0.442	Hart & Dunn (1993)
Y	0.467	Hart & Dunn (1993)
Ho	0.44	Paster *et al.* (1974)
Er	0.39	Hart & Dunn (1993)
Yb	0.43	Hart & Dunn (1993)
Lu	0.433	Hart & Dunn (1993)

Equilibrium melt compositions

Trace element compositions of parental melts to the xenoliths were calculated using basalt-clinopyroxene partition coefficients (Kds). The Kds are given in Table 4 and plotted in the Supplemental Data. Average calculated equilibrium melt compositions for each group are shown in Fig. 11 and given in the Supplemental Data.

Group 1: The equilibrium melt compositions for Group 1 clinopyroxene are within the adakite field as defined by Castillo (2012) and others (Supplemental Data Figure S11). Adakite lavas from the Santa Clara volcanic field in Baja (Aguillón-Robles *et al.*, 2001) show remarkably similar trace element systematics to this group in terms of La/Yb ratios (14–32) and Sr enrichment (Sr/Y 62–164), although with notably higher Th, U, and HFSE concentrations (Fig. 11a). Group 1 melt compositions are also broadly similar to high-Mg andesite ADK-53 from Adak Island (Sun, 1980; Kay *et al.*, 1986; Münker *et al.*, 2004). Although the absolute concentrations of most trace elements are higher in ADK-53 (e.g. 1780 μg/g Sr), the sample shows a similar degree of LREE-HREE fractionation (La/Yb 30–31) and HFSE depletion (Nb/La = 0.1, Zr/Zr∗ = 0.27). The trace element similarities between our calculated melt compositions and these adakites support our hypothesis that a basaltic eclogite melt contributed to the parental magmas of the most primitive Moffett xenoliths.

Group 2: Melt compositions calculated from the Group 2 clinopyroxene are generally depleted in all trace elements (Fig. 11a). While these compositions still show significant LREE-HREE fractionation (La/Yb 8–12), Sr enrichment (Sr/Sr∗ 2.5–2.9), and HFSE depletion (Zr/Zr∗ 0.25–0.66), they do not meet the

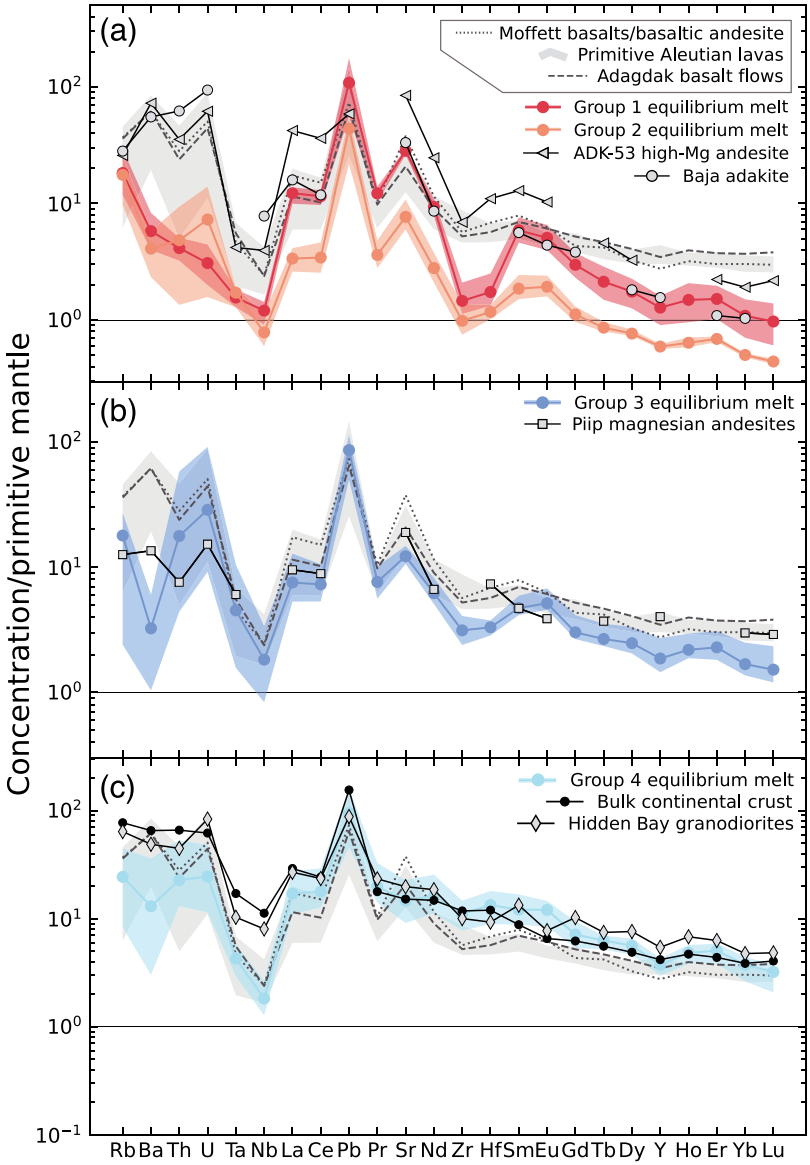

Fig. 11. Equilibrium melt compositions calculated from clinopyroxene trace element concentrations, sorted by compositional group. Solid lines represent group averages and shaded areas represent the variations observed in equilibrium melt compositions from each group. Whole rock trace element data of Adagdak basalt flows (dashed lines) and Moffett basalts and basaltic andesites (dotted lines) are shown for comparison (Marsh, 1976; Kay & Kay, 1994). The compilation of primitive Aleutian calc-alkaline basalts and andesites from Schmidt & Jagoutz (2017) is represented by the gray field. (a) Groups 1 and 2 equilibrium melt compositions. Whole rock data from adakite ADK-53 (Adak Island, Sun, 1980; Kay *et al.*, 1986; Kay & Kay, 1994; Münker *et al.*, 2004) and adakites from the Santa Clara volcanic field, Baja California (Aguillón-Robles *et al.*, 2001) is given for comparison. (b) Group 3 equilibrium melt compositions. Data from Piip volcano magnesian andesites (Yogodzinski *et al.*, 1994) is shown for comparison. (c) Group 4 equilibrium melt compositions. Whole rock data from the Hidden Bay pluton (Kay *et al.*, 1990, 2019) is also shown.

required criteria to be classified as 'adakites' (e.g. Sr > 300 μg/g: Castillo, 2012).

Group 3: Calculated equilibrium melt compositions for Group 3 clinopyroxene show more modest LREE-HREE fractionation (La/Yb 5–12) and Sr enrichment (Sr/Sr∗ 1.9–2.8) than those from Groups 1 and 2 and are more akin to typical Aleutian calc-alkaline basalts (Fig. 11b). Absolute HREE concentrations in Group 3 equilibrium melts are lower, but within error, of previously identified primitive melts from the Aleutians (Kay *et al.*, 1982; Kay & Kay, 1994; and Schmidt & Jagoutz, 2017; Fig. 11). Group 3 equilibrium melt compositions are similar to magnesian andesites from Piip volcano in the western Aleutians (Yogodzinski *et al.*, 1994). Yogodzinski *et al.* (1994) proposed a model for the petrogenesis of Piip magnesian andesites where a low-degree slab melt stalls in the subarc mantle, creating an enriched source rock. Subsequent melting of this hybridized peridotite then produces basalts with trace element characteristics inherited from the original slab melt. Because these signatures are less pronounced in the Group 3 melts (e.g. less HREE-LREE fractionation, lower Sr), and the mineralogy of ultramafic xenoliths from this group suggests fractionation from a primitive basalt, a similar petrogenic scenario may be appropriate for this group: hybridization or mixing of silicic basaltic eclogite derived magmas and mantle peridotite/melts.

Group 4: Group 4 equilibrium melts show the least LREE-HREE fractionation (La/Yb 4–10) and HFSE depletion (Zr/Zr∗ 0.5–1.45: Fig. 11c). Melt compositions calculated for five samples in this group show negative Sr-anomalies (Sr/Sr∗ 0.8 to 0.9), in contrast

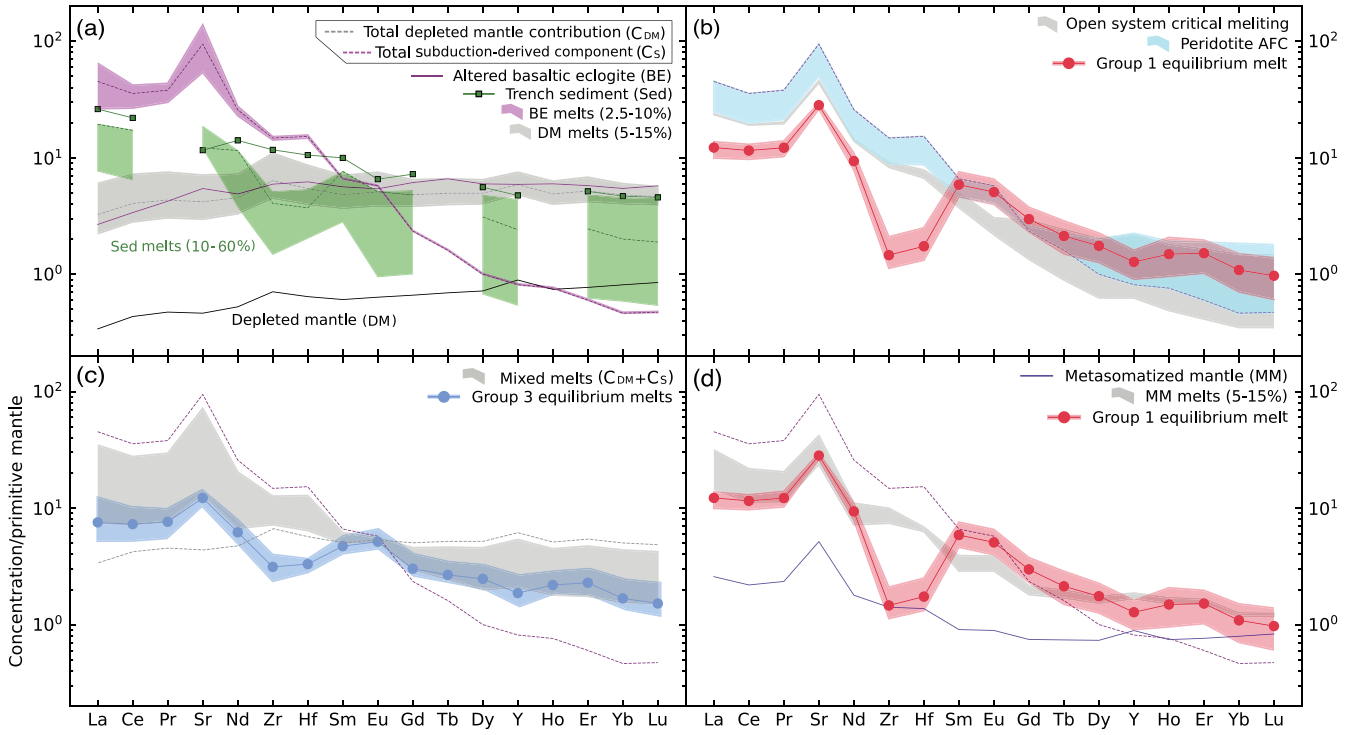

Fig. 12. Trace element modeling results. Group 1, and 3 melt compositions overlay model results that give best fits. (a) Compositions of source rocks and melts used in modeling. Dotted lines represent the subduction-derived and mantle melt compositions used in models, while shaded fields represent compositional variations for different degrees of basaltic eclogite and mantle melting. (b) Model results for subduction-derived melt reacting with the depleted mantle through AFC reactions (DePaolo, 1981) and open system critical melting (Shaw, 2000). (c) Model results for mixing subduction-derived melt with 10% depleted mantle melt. (d) Model results for 5% to 10% melting of a mantle composition modally metasomatized by a subduction-derived melt in a 1:9 melt/rock ratio.

to groups 1–3, due to the co-crystallization of clinopyroxene with plagioclase. Group 4 equilibrium melts are similar to the bulk compositions of non-cumulate granodiorites from Adak's Hidden Bay pluton (Kay *et al.*, 1983, 1990, 2019) (Fig. 11c). Kay *et al.* (2019) suggest a model for the formation of the Hidden Bay pluton in which a high-Al basalt ascends to mid-crustal depths (11–13 km) and fractionates the cumulate gabbro and diorite units. The granodiorite and leucogranodiorite units then formed during further crystallization of the residual magma in the upper crust (2–4 km). A similar mid-crustal origin from an evolved basalt or basaltic andesite may be an appropriate petrogenic model for the Group 4 cumulates.

Modeling the origin of parental melts to the Adak xenoliths

The trace element systematics of our equilibrium melt compositions for Groups 1–3 show similarities to those produced by melting experiments of basaltic eclogites (Rapp *et al.*, 1999; Sisson & Kelemen, 2018) and sediments (Hermann & Spandler, 2008; Mallik *et al.*, 2015, 2016); however, these experimental partial melts are also characterized by high-silica contents (Ringwood, 1990; Rapp *et al.*, 1991, 1999; Sen & Dunn, 1994; Rapp & Watson, 1995; Johnson & Plank, 1999; Hermann & Rubatto, 2009). Thus, interaction between basaltic eclogite and mantle melts or peridotite was critical to the origin of the parental melts to the most primitive cumulates. In this section, we model and explore interactions between melts of the depleted mantle, basaltic eclogites, and subducted sediments. All partition coefficients, melting modes, source rock compositions, and modal proportions used are given in the Supplemental Data. The models given below represent end-member scenarios, none of which fully reproduce all characteristics of our data, and all of which require assumptions about the subarc mantle beneath Adak. We emphasize that it is likely that several of these processes were operating contemporaneously. We focus on the elements most relevant for exploring these interactions and for which our equilibrium melt calculations are the most robust (i.e. elements present in clinopyroxene in concentrations well above detection limits, with well-constrained mineral-melt partition coefficients for all required phases).

Model components

Depleted mantle melt: We implement a non-modal batch melting model (Kinzler & Grove, 1992, using equations of Shaw, 2006) and the depleted mantle composition of Salters & Stracke (2004). Calculated equilibrium melts for 5% to 15% depleted mantle partial melting are shown in Figure 12a.

Basaltic eclogite melt: We modeled non-modal fractional melting of a basaltic eclogite with an altered oceanic composition. Results for 2.5–10% partial melting of a basaltic eclogite are shown in Fig. 12a. All modeled melts display positive Sr anomalies (Sr/Sr^* 2.0–3.9) and extreme LREE-HREE fractionation (La/Yb 70–190).

Sediment melt: The metamorphism of subducted sediment may result in the formation of many incompatible element-rich accessory phases including garnet, amphibole, biotite, magnetite, coesite, kyanite, apatite, zircon, phengite, allanite, and monazite (Johnson & Plank, 1999; Hermann & Spandler, 2008; Skora & Blundy, 2010). Partial melting (10–60%) experiments of trench sediments under conditions relative to the top of subducting slabs (600–900°C, 2–4.5 GPa) have produced hydrous rhyolitic to

basaltic melts with highly variable trace element compositions (Johnson & Plank, 1999; Hermann & Spandler, 2008; Hermann & Rubatto, 2009; Skora & Blundy, 2010). This means that minor variations in metasedimentary phase assemblages and slab-top P–T–H_2O–fO_2 can significantly affect trace element partitioning between residues and melts. We, therefore, calculated a range of possible Aleutian sediment melt compositions using an array of bulk sediment-melt partition coefficients (Johnson & Plank, 1999) (Fig. 12a). We take the melt composition calculated using the 700°C (experiment PC36) bulk partition coefficients from Johnson & Plank (1999) as our sediment-melt component. This set of partition coefficients was chosen because (a) it is roughly the temperature at which the solidus for subducted sediment (Nichols *et al.*, 1994; Hermann & Spandler, 2008) crosses the slab-top geotherm for the central Aleutians (Syracuse *et al.*, 2010) (Supplemental Data Figure S1) and (b) the melt composition calculated using these partition coefficients is close to the average of our range of possible sediment melt field. We add this sediment melt component to the 5% basaltic eclogite melt in a 1:19 sediment: basaltic eclogite melt ratio, hitherto referred to as the 'subduction-derived component' in all subsequent modeling (Fig. 12a).

We explore three possible scenarios of how our subduction-derived components interact with depleted mantle melts or peridotite to form mafic to intermediate magmas with slab-derived trace element signatures: (1) reactions between mantle peridotite and subduction-derived melts; (2) mixing of subduction-derived and depleted mantle melts; and (3) metasomatism of the depleted mantle by a subduction-derived melt, followed by partial melting of the hybridized mantle.

(1) *Reactions between mantle peridotite and basaltic eclogite melts*

Experimental studies have demonstrated that reactions between basaltic eclogite melts and mantle peridotite provide an effective means for silicic magmas to develop more primitive major element characteristics while maintaining their highly fractionated trace element patterns. For example, Rapp *et al.* (1999) found that when a dacitic partial melt of an eclogite reacted with depleted peridotite in a 2:1 melt/rock ratio, melt SiO_2 concentrations decreased from 67.5 to 61.1 wt % and Mg# increased from 44 to 56. These changes in major element composition were accompanied by only minor changes in trace element concentrations (e.g. Y decreased from 6.7 to 5.8 μg/g, Yb increased from 0.9 to 1.3 μg/g; Rapp *et al.*, 1999).

We first explore reactions between our subduction-derived melt and mantle peridotite with the AFC model of DePaolo (1981). We modeled a scenario in which the rate of assimilation of mantle peridotite is greater than the rate of crystallization, and the mass of the magma increases during assimilation. As the melt mass increases, it acquires characteristics of the peridotite it consumes, resulting in a general decrease in the degree of LREE/HREE fractionation in the hybridized melts. In general, the AFC model results provide a good fit for our Group 1 melt compositions (Fig. 12b). We also implemented an open-system critical melting model (Shaw, 2000), in which peridotite is melted at the same time as a subduction-derived melt is added to the system, while a hybridized melt is expelled. The more subduction-derived melt is added, the less effect the peridotite melt has on the expelled hybridized magma composition, consistent with channelized ascent. Interaction with peridotite is primarily observed in the HREEs, which are closer to mantle values when small quantities of melt are reacted with peridotite. The model results for the open-system critical melting also reproduce the HREE depletions observed in the Group 1 melt compositions (Fig. 12b). Based on these results, we consider reactions between subduction-derived melts and mantle peridotite a viable mechanism for the petrogenesis of the parental melts to our Group 1 xenoliths.

(2) *Mixing of basaltic eclogite and mantle melts.*

Previous studies have also evoked mixing between basaltic eclogite melts and mantle magmas to explain the geochemistry of mafic to intermediate arc lavas and their phenocrysts (e.g. Mount Shasta: Streck *et al.*, 2007; Northern Andean Volcanic zone: Schiano *et al.*, 2010). We used a simple binary mixing model to combine our subduction-derived melt with a 10% mantle melt over a 1:3 to 3:1 subduction-derived/mantle melt ratio (Fig. 12c). Although we explore magma mixing over a large range of mixing ratios, the modeled compositions containing over a 50% subduction-derived melt component would be overly silicic. These model results provide a reasonable fit for some of our less fractionated Group 3 melts (Fig. 12c). While experimental and modeling studies have shown that silicic and mafic melts might not readily mix due to viscosity differences (Campbell & Turner, 1985; Sparks & Marshall, 1986), mixing of felsic and mafic melts in the upper mantle or lower crust may be possible, given sufficient time under an appropriate thermal regime and in the presence of water. If water-saturated basaltic eclogite melts are sufficiently heated as they ascend through the inverted geothermal gradient of the lower mantle wedge, or if such a high-silica melt is added slowly to the mantle melt, the viscosity of the basaltic eclogite melt may approach that of a mantle basalt, facilitating mixing.

(3) *Partial melting of metasomatized mantle.*

Metasomatism of mantle peridotite by a basaltic eclogite melt, followed by partial melting of the hybridized rock, may be an appropriate petrogenic model when the degree of basaltic eclogite melting is low (Rapp *et al.*, 1999). To illustrate this, we generated a bulk metasomatized peridotite composition by mixing our subduction-derived melt with a depleted mantle composition with a melt: rock ratio ranging from 1:9 to 1:1. These new mantle compositions display greater LREE/HREE fractionation (La/Yb 2.3–25) than the original depleted source (La/Yb 0.6), as well as positive Sr anomalies (Sr/Sr$*$ 2.2 to 2.9) (Supplemental Data Figure S12). Experimental studies have shown that reactions between basaltic eclogite melts and peridotite often result in precipitation of orthopyroxene, amphibole, and garnet and consumption of olivine (Sekine & Wyllie, 1982; Johnston & Wyllie, 1989; Sen & Dunn, 1995; Rapp *et al.*, 1999). We, therefore, modeled 5% to 15% melting of a garnet-amphibole peridotite with each of our metasomatized mantle compositions. The best match for our Group 1 melt compositions was produced through ~10% melting of a modally metasomatized mantle composition generated through reactions between our subduction-derived melt and the depleted mantle in a 1:9 melt/rock ratio (Fig. 12d).

Modeling conclusions

The strongly fractionated trace element characteristics of the equilibrium melts for the Group 1 xenoliths require a significant contribution (>5%) from a basaltic eclogite melt. This is consistent with the recent study of Turner & Langmuir (2022a), which suggests a 5% to 7% slab melt component is ubiquitous in convergent margin magmas. Reactions between a basaltic eclogite melt and peridotite (Fig. 12b), or partial melting of a metasomatized mantle (Fig. 12d) may have been important processes in the petrogenesis of the parental melts to these samples. The parental melts to the Group 3 cumulates may have formed through mixing of slab and mantle melts (Fig. 12c) or partial melting of a less metasomatized mantle. All three models fail, however, to reproduce the Zr and

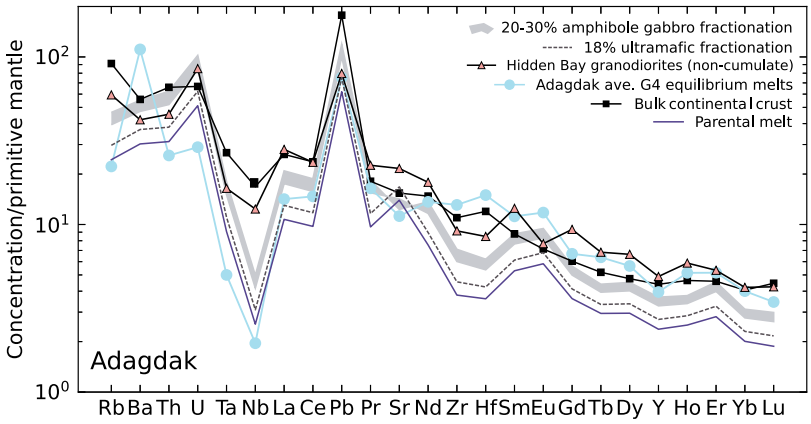

Fig. 13. Trace element fractional crystallization model results for Adagdak. Bulk continental crust composition is from Rudnick & Gao (2003) and Hidden Bay pluton data is from Kay *et al.* (2019).

Hf depletions observed in Groups 1 and 2 melt compositions. Previous studies have suggested that in addition to rutile, zircon may be an important phase in controlling the HSFE budget of subduction zones (Rubatto & Hermann, 2003; Hirai *et al.*, 2018; Turner & Langmuir, 2022a). Zircon has also been observed in the residues of partial melting experiments of metasedimentary rocks (Johnson & Plank, 1999; Rubatto & Hermann, 2003). The depletions in Hf and Zr observed in the calculated equilibrium melt compositions could, therefore, reflect the presence of zircon in their melting residues (basaltic eclogites and/or metasediments).

These results can be interpreted two ways: (1) the mantle beneath Adak is heterogenous, with Adagdak and Moffett volcanoes sampling melts generated in regions of the mantle that have experienced variable degrees of interaction with a subduction-derived component, or (2) if the Moffett and Adagdak cumulates are not contemporaneous, the dynamics of the mantle source region beneath Adak may have changed in the elapsed time between the crystallizations of the two separate cumulate suites (Supplemental Data Figure S13). Temporal changes in the strength of the basaltic eclogite melt signature, particularly if the changes correlate to periods of arc migration, may suggest that the source of these signatures is forearc subduction erosion. Testing these hypotheses requires high-precision chronology of cumulates, which is beyond the scope of this paper.

Relationship to upper crustal plutonic rocks on Adak

A notable feature of all models explored above is that the positive Sr-anomaly of the original slab-derived component persists in melt compositions produced through peridotite–eclogite melt interactions. This finding has been emphasized by previous models of peridotite–eclogite melt reactions (Sisson & Kelemen, 2018). Positive Sr-anomalies are typical features of primitive arc magmas including basalts (Perfit *et al.*, 1980; Kelemen *et al.*, 2003b; Schmidt & Jagoutz, 2017; Turner & Langmuir, 2022a) and adakites (Kay, 1978; Kay *et al.*, 1986; Yogodzinski *et al.*, 1994). However, as arc magmatism is thought to be the primary mechanism by which continental crust is generated, a conundrum arises in that the average bulk continental crust has a Sr/Sr∗ value of 0.94 (preferred value of Rudnick & Gao, 2003). Furthermore, the upper continental crust has a slightly negative estimated Sr/Sr∗ of 0.67. This implies that if magmas with positive Sr anomalies are parental to the continental crust, (intra-) crustal processes must erase the primary positive Sr anomalies of primitive arc magmas. Removal of excess Sr could occur through differentiation of plagioclase-bearing cumulates, which could eventually be removed via density foundering (Kay & Mahlburg-Kay, 1991; Kay & Mahlburg Kay, 1993; Kelemen *et al.*, 2003b; Jagoutz & Schmidt, 2013). This process is consistent with observations from preserved paleo-arcs where densification reactions involving the transformation of plagioclase (+ olivine) to produce garnet, pyroxene, and spinel are observed (e.g. Kohistan: Jagoutz & Schmidt, 2013). Alternatively, Sr may be preferentially lost from the crust during chemical weathering (Rudnick, 1995; Rudnick & Gao, 2003).

We use the xenolith suite studied here and the upper crustal plutonic rocks from Adak (namely the calc-alkaline Hidden Bay pluton, Kay *et al.*, 1990, 2019) to understand the differentiation process within the arc and the evolution of Sr anomalies in near-primitive melts with a strong basaltic eclogite melt component. We model fractional crystallization of Adagdak and Moffett primitive melts through stepwise removal of calculated bulk cumulate trace element assemblages (see Supplemental Data for details). For Adagdak, this consisted of removing 18% of an ultramafic assemblage and 30% of a gabbroic assemblage from our most primitive equilibrium melt composition. The results of this modeling are shown in Figure 13. Fractionation of the Adagdak ultramafic cumulates results in increased concentrations of all trace elements in the remaining liquid with little modification to Sr-anomalies (Sr/Sr∗ 1.60–1.61). Once amphibole gabbro fractionation begins, and we remove Sr-rich plagioclase-bearing lithologies, Sr-anomalies begin to decline and are absent after 22% amphibole gabbro fractionation (Sr/Sr∗ = 1). After 30% amphibole gabbro fractionation, Sr-anomalies are in fact negative (Sr/Sr∗ = 0.76). Another notable feature of the model is that the final compositions are very similar to non-cumulate granodiorite assemblages from the Hidden Bay pluton on Adak Island (Fig. 13). While most of the Hidden Bay diorites are interpreted as cumulates, some of the granodiorites and leucogranodiorites are thought to represent the magmatic compositions (Kay *et al.*, 2019). We further screened the granodiorite compositions from Kay *et al.* (2019) to remove compositions showing signs of plagioclase accumulation (Sr/Sr∗ and Eu/Eu∗ > 1).

We employed the same method for studying the Moffett suite, starting with the equilibrium melt composition for our most primitive cumulates (MM-CB-2) and removing representative cumulate assemblages through a mass balance model (see Supplemental Data for details). Because the Sr concentrations in these melt compositions are very high (>500 μg/g), fractionation of

lower Sr phases like clinopyroxene (30–80 μg/g Sr) and amphibole (230–350 μg/g Sr) serves to increase Sr in the remaining melt. By the time plagioclase-bearing assemblages began to fractionate, Sr concentrations in the remaining melt were > 600 μg/g. Although Moffett amphibole gabbros have high (~400 to 600 μg/g) Sr, even after 30% fractionation, strong positive Sr-anomalies remained (Sr/Sr* decreased from 2.01 to 1.50, Supplemental Data Figure S15).

Although undoubtedly an oversimplification, these results suggest that (1) the trace element chemistry of the Adagdak cumulate suite can be related to that of the non-cumulate Hidden Bay plutonic rocks through fractional crystallization, and the cumulates may represent lower crustal complements to the Hidden Bay granodiorites, and (2) the loss of positive Sr-anomalies from primitive arc lavas to their more evolved, intrusive equivalents may be achieved by fractionation of plagioclase bearing lithologies. With respect to Moffett, these results suggest that Sr-anomalies in melts with strong basaltic eclogite melt components may persist throughout differentiation, even when plagioclase is part of the fractionated assemblage. The diminution of Sr-anomalies within the Adagdak fractionation suite affirms the idea that reconciling geochemical differences between arc magmas (and their crystallization product), with estimates of the bulk continental crust, can be achieved through the removal of plagioclase-rich cumulates through densification reactions.

CONCLUSION

The petrography and mineral chemistry of primitive cumulates from Moffett and Adagdak volcanoes are consistent with fractionation from hydrous, oxidized parental melts in the upper mantle or lower crust, however important differences exist. Primitive cumulates from both suites are distinct from those in arcs where the slab-derived component has previously been attributed to an aqueous fluid (e.g. Lesser Antilles), but are similar to those from locations where the parental melt has been interpreted to contain a slab-derived component (e.g. Kamchatka). This relationship suggests that the parental melts to the most primitive Adak cumulates contain a basaltic eclogite melt component from slab melting and/or forearc subduction erosion.

Clinopyroxenes from the most primitive cumulates in both suites display positive Sr anomalies, which are not observed in the more evolved lithologies. The loss of the positive Sr anomaly can be modeled through fractionation of plagioclase-bearing cumulates for the Adagdak suite. However, the differences between the pronounced Sr anomalies and depletions in HREEs and HSFEs observed in the most primitive Moffett samples cannot be reconciled with the relatively unfractionated trace element patterns observed in the more evolved samples. This relationship suggests that supracrustal processes, or injection of a compositionally distinct basaltic melt, may be an important process for the Moffett volcanic system. Together, the differences in major and trace element systematics between the two xenolith suites suggest a complex magma plumbing system beneath Adak Island, with the two volcanoes either tapping a heterogenous mantle source characterized by variable degrees of interaction with an eclogite melt or a mantle source region that has chemically evolved through time.

DATA AVAILABILITY STATEMENT

Supplemental data for this article are available from the Journal of Petrology website.

Supplementary Data

Supplementary data are available at Journal of Petrology online.

ACKNOWLEDGEMENTS

We thank C. Ma and L. Saper for their assistance with electron microprobe analyses, L.V. Godfrey for her assistance with the LA-ICP-MS, and B. Wood for providing the spinel standards. Constructive reviews from T.W. Sisson and an anonymous reviewer significantly improved the quality of the manuscript and are gratefully acknowledged. E.S.S. was supported by the National Science Foundation Graduate Research Fellowship under Grant No. DGE-1745301. Special thanks to T.L. Carley and the Lafayette College Department of Geology and Environmental Geosciences for the use of their petrographic microscopes, which allowed this work to continue during the COVID-19 pandemic.

References

Abe, N., Arai, S. & Yurimoto, H. (1998). Geochemical characteristics of the uppermost mantle beneath the Japan island arcs: implications for upper mantle evolution. *Physics of the Earth and Planetary Interiors* **107**, 233–248. https://doi.org/10.1016/S0031-9201(97)00136-2.

Aguillón-Robles, A., Calmus, T., Benoit, M., Bellon, H., Maury, R. C., Cotten, J., Bourgois, J. & Michaud, F. (2001). Late Miocene adakites and Nb-enriched basalts from Vizcaino Peninsula, Mexico: indicators of East Pacific Rise subduction below southern Baja California? *Geology* **29**, 531. https://doi.org/10.1130/0091-7613(2001)029<0531:LMAANE>2.0.CO;2.

Ballhaus, C., Berry, R. F. & Green, D. H. (1991). High pressure experimental calibration of the olivine-orthopyroxene-spinel oxygen geobarometer: implications for the oxidation state of the upper mantle. *Contributions to Mineralogy and Petrology* **107**, 27–40. https://doi.org/10.1007/BF00311183.

Baten, Soyini, K. (2002) *Eruptive History and Assessment of Volcanic Hazards of Mt. Adagdak, Adak Island, Aleutian Islands, Alaska* Unpublished Ph.D. thesis. Northern Arizona University.

Beyer, B. J. (1980) *Petrology and geochemistry of ophiolite fragments in a tectonic melange, Kodiak Islands, Alaska*Unpublished Ph.D. thesis,. Santa Cruz: University of California.

Bezard, R., Turner, S., Schaefer, B., Yogodzinski, G. & Hoernle, K. (2021). Os isotopic composition of western Aleutian adakites: implications for the re/Os of oceanic crust processed through hot subduction zones. *Geochimica et Cosmochimica Acta* **292**, 452–467. https://doi.org/10.1016/j.gca.2020.10.009.

Blatter, D. L., Sisson, T. W. & Hankins, W. B. (2013). Crystallization of oxidized, moderately hydrous arc basalt at mid- to lower-crustal pressures: implications for andesite genesis. *Contributions to Mineralogy and Petrology* **166**, 861–886. https://doi.org/10.1007/s00410-013-0920-3.

Blatter, D. L., Sisson, T. W. & Hankins, W. B. (2017). Voluminous arc dacites as amphibole reaction-boundary liquids. *Contributions to Mineralogy and Petrology* **172**, 1–37. https://doi.org/10.1007/s00410-017-1340-6.

Bourgois, J., Martin, H., Lagabrielle, Y., Le Moigne, J. & Frutos Jara, J. (1996). Subduction erosion related to spreading-ridge subduction: Taitao peninsula (Chile margin triple junction area). *Geology* **24**, 723–726. https://doi.org/10.1130/0091-7613(1996)024<0723:SERTSR>2.3.CO;2.

Brounce, M. N., Kelley, K. A. & Cottrell, E. (2014). Variations in Fe3+/$\sum$Fe of Mariana Arc basalts and mantle wedge fO2.

Journal of Petrology **55**, 2513–2536. https://doi.org/10.1093/petrology/egu065.

Bryant, J. A., Yogodzinski, G. M. & Churikova, T. G. (2007). Melt-mantle interactions beneath the Kamchatka arc: evidence from ultramafic xenoliths from Shiveluch volcano. *Geochemistry, Geophysics, Geosystems* **8**. https://doi.org/10.1029/2006GC001443.

Bryndzia, L. T. & Wood, B. J. (1990). Oxygen thermobarometry of abyssal spinel peridotites; the redox state and C-O-H volatile composition of the Earth's sub-oceanic upper mantle. *American Journal of Science* **290**, 1093–1116. https://doi.org/10.2475/ajs.290.10.1093.

Bucholz, C. E. & Kelemen, P. B. (2019). Oxygen fugacity at the base of the Talkeetna arc, Alaska. *Contributions to Mineralogy and Petrology* **174**, 79. https://doi.org/10.1007/s00410-019-1609-z.

Campbell, I. H. & Turner, J. S. (1985). Turbulent mixing between fluids with different viscosities. *Nature* **313**, 39–42. https://doi.org/10.1038/313039a0.

Castillo, P. R. (2012). Adakite petrogenesis. *Lithos* **134-135**, 304–316. https://doi.org/10.1016/j.lithos.2011.09.013.

Cawthorn, R. G., Curran, E. B. & Arculus, R. J. (1973). A Petrogenetic model for the origin of the Calc-alkaline suite of Grenada, Lesser Antilles. *Journal of Petrology* **14**, 327–337. https://doi.org/10.1093/petrology/14.2.327.

Citron, G. P., Kay, R. W., Kay, S. M., Snee, L. W. & Sutter, J. F. (1980). Tectonic significance of early Oligocene plutonism on Adak Island, Central Aleutian Islands, Alaska. *Geology* **8**, 375–379. https://doi.org/10.1130/0091-7613(1980)8<375:TSOEOP>2.0.CO;2.

Coats, R. R. (1956). Geology of northern Adak Island, Alaska. *US Geological Survey Bulletin* **1028-C**, 45–67.

Conrad, W. K. & Kay, R. W. (1984). Ultramafic and mafic inclusions from Adak Island: crystallization history and implications for the nature of primary magmas and crustal evolution in the Aleutian arc. *Journal of Petrology* **25**, 88–125. https://doi.org/10.1093/petrology/25.1.88.

Conrad, W. K., Kay, S. M. & Kay, R. W. (1983). Magma mixing in the Aleutian arc: evidence from cognate inclusions and composite xenoliths. *Journal of Volcanology and Geothermal Research* **18**, 279–295. https://doi.org/10.1016/0377-0273(83)90012-4.

Cooper, G. F., Davidson, J. P. & Blundy, J. D. (2016). Plutonic xenoliths from Martinique, Lesser Antilles: evidence for open system processes and reactive melt flow in island arc crust. *Contributions to Mineralogy and Petrology* **171**, 87. https://doi.org/10.1007/s00410-016-1299-8.

Cottrell, E. & Kelley, K. A. (2011). The oxidation state of Fe in MORB glasses and the oxygen fugacity of the upper mantle. *Earth and Planetary Science Letters* **305**, 270–282. https://doi.org/10.1016/j.epsl.2011.03.014.

Cottrell, E., Birner, S. K., Brounce, M., Davis, F. A., Waters, L. E. & Kelley, K. A. (2021). Oxygen fugacity across tectonic settings. *Magma redox geochemistry* , 33–61. https://doi.org/10.1002/9781119473206.ch3.

Davies, J. H. & Stevenson, D. J. (1992). Physical model of source region of subduction zone volcanics. *Journal of Geophysical Research: Solid Earth* **97**, 2037–2070. https://doi.org/10.1029/91JB02571.

Davis, F. A., Cottrell, E., Birner, S. K., Warren, J. M. & Lopez, O. G. (2017). Revisiting the electron microprobe method of spinel-olivine-orthopyroxene oxybarometry applied to spinel peridotites. *American Mineralogist* **102**, 421–435. https://doi.org/10.2138/am-2017-5823.

DeBari, S. M. & Coleman, R. G. (1989). Examination of the deep levels of an island arc: evidence from the Tonsina ultramafic–mafic assemblage, Tonsina, Alaska. *Journal of Geophysical Research: Solid Earth* **94**, 4373–4391. https://doi.org/10.1029/JB094iB04p04373.

Debari, S., Kay, S. M. & Kay, R. W. (1987). Ultramafic xenoliths from Adagdak Volcano, Adak, Aleutian Islands, Alaska: deformed igneous cumulates from the Moho of an island arc. *The Journal of Geology* **95**, 329–341. https://doi.org/10.1086/629133.

Defant, M. J. & Drummond, M. S. (1990). Derivation of some modern arc magmas by melting of young subducted lithosphere. *Nature* **347**, 662–665. https://doi.org/10.1038/347662a0.

DePaolo, D. J. (1981). Trace element and isotopic effects of combined wallrock assimilation and fractional crystallization. *Earth and Planetary Science Letters* **53**, 189–202. https://doi.org/10.1016/0012-821X(81)90153-9.

Dohmen, R., Faak, K. & Blundy, J. D. (2017). Chronometry and Speedometry of magmatic processes using chemical diffusion in olivine, plagioclase and pyroxenes. *Reviews in Mineralogy and Geochemistry* **83**, 535–575. https://doi.org/10.2138/rmg.2017.83.16.

Drummond, M. S. & Defant, M. J. (1990). A model for Trondhjemite–Tonalite–Dacite Genesis and crustal growth via slab melting: Archean to modern comparisons. *Journal of Geophysical Research: Solid Earth* **95**, 21503–21521. https://doi.org/10.1029/JB095iB13p21503.

Fraser, G. D. & Snyder, G. L. (1959). Geology of southern Adak Island and Kagalaska Island, Alaska. *US Geological Survey Bulletin* **1028-M**, 371–408.

Gaetani, G. A., Grove, T. L. & Bryan, W. B. (1993). The influence of water on the petrogenesis of subduction related igneous rocks. *Nature* **365**, 332–334. https://doi.org/10.1038/365332a0.

Geist, E. L., Childs, J. R. & Scholl, D. W. (1988). The origin of summit basins of the Aleutian ridge: implications for block rotation of an arc massif. *Tectonics* **7**, 327–341. https://doi.org/10.1029/TC007i002p00327.

Goss, A. R. & Kay, S. M. (2006). Steep REE patterns and enriched Pb isotopes in southern central American arc magmas: evidence for forearc subduction erosion? *Geochemistry, Geophysics, Geosystems* **7**. https://doi.org/10.1029/2005GC001163.

Goss, A. R., Kay, S. M. & Mpodozis, C. (2013). Andean Adakite-like high-Mg Andesites on the northern margin of the Chilean–Pampean flat-slab (27–28·5°S) associated with frontal arc migration and fore-arc subduction erosion. *Journal of Petrology* **54**, 2193–2234. https://doi.org/10.1093/petrology/egt044.

Green, T. H. & Ringwood, A. E. (1968). Genesis of the calc-alkaline igneous rock suite. *Contributions to Mineralogy and Petrology* **18**, 105–162. https://doi.org/10.1007/BF00371806.

Greene, A. R., DeBari, S. M., Kelemen, P. B., Blusztajn, J. & Clift, P. D. (2006). A detailed geochemical study of island arc crust: the Talkeetna arc section, south–Central Alaska. *Journal of Petrology* **47**, 1051–1093. https://doi.org/10.1093/petrology/egl002.

Gust, D. A. & Perfit, M. R. (1987). Phase relations of a high-Mg basalt from the Aleutian Island Arc: implications for primary island arc basalts and high-Al basalts. *Contributions to Mineralogy and Petrology* **97**, 7–18. https://doi.org/10.1007/BF00375210.

Hart, S. R. & Dunn, T. (1993). Experimental cpx/melt partitioning of 24 trace elements. *Contributions to Mineralogy and Petrology* **113**, 1–8. https://doi.org/10.1007/BF00320827.

Hauri, E. H., Wagner, T. P. & Grove, T. L. (1994). Experimental and natural partitioning of Th, U, Pb and other trace elements between garnet, clinopyroxene and basaltic melts. *Chemical Geology* **117**, 149–166. https://doi.org/10.1016/0009-2541(94)90126-0.

Helz, R. T. (1973). Phase relations of basalts in their melting range at PH2O = 5 kb as a function of oxygen fugacity1: part I. mafic phases. *Journal of Petrology* **14**, 249–302. https://doi.org/10.1093/petrology/14.2.249.

Hermann, J. & Rubatto, D. (2009). Accessory phase control on the trace element signature of sediment melts in subduction

zones. *Chemical Geology* **265**, 512–526. https://doi.org/10.1016/j.chemgeo.2009.05.018.

Hermann, J. & Spandler, C. J. (2008). Sediment melts at sub-arc depths: an experimental study. *Journal of Petrology* **49**, 717–740. https://doi.org/10.1093/petrology/egm073.

Hirai, Y., Yoshida, T., Okamura, S., Tamura, Y., Sakamoto, I. & Shinjo, R. (2018). Breakdown of residual zircon in the Izu arc subducting slab during backarc rifting. *Geology* **46**, 371–374. https://doi.org/10.1130/G39856.1.

Holland, T. & Blundy, J. (1994). Non-ideal interactions in calcic amphiboles and their bearing on amphibole-plagioclase thermometry. *Contributions to Mineralogy and Petrology* **116**, 433–447. https://doi.org/10.1007/BF00310910.

Holloway, J. R. & Burnham, C. W. (1972). Melting relations of basalt with equilibrium water pressure less than Total Pressure1. *Journal of Petrology* **13**, 1–29. https://doi.org/10.1093/petrology/13.1.1.

von Huene, R. & Scholl, D. W. (1991). Observations at convergent margins concerning sediment subduction, subduction erosion, and the growth of continental crust. *Reviews of Geophysics* **29**, 279–316. https://doi.org/10.1029/91RG00969.

Ichiyama, Y., Morishita, T., Tamura, A. & Arai, S. (2016). Peridotite xenoliths from the Shiribeshi Seamount, Japan Sea: insights into mantle processes in a back-arc basin. *Contributions to Mineralogy and Petrology* **171**, 86. https://doi.org/10.1007/s00410-016-1300-6.

Ishimaru, S., Arai, S., Ishida, Y., Shirasaka, M. & Okrugin, V. M. (2006). Melting and multi-stage Metasomatism in the mantle wedge beneath a frontal arc inferred from highly depleted peridotite xenoliths from the Avacha Volcano, Southern Kamchatka. *Journal of Petrology* **48**, 395–433. https://doi.org/10.1093/petrology/egl065.

Jagoutz, O. & Schmidt, M. W. (2013). The composition of the foundered complement to the continental crust and a re-evaluation of fluxes in arcs. *Earth and Planetary Science Letters* **371-372**, 177–190. https://doi.org/10.1016/j.epsl.2013.03.051.

Jagoutz, O., Müntener, O., Ulmer, P., Pettke, T., Burg, J.-P., Dawood, H. & Hussain, S. (2007). Petrology and mineral chemistry of lower crustal intrusions: the Chilas Complex, Kohistan (NW Pakistan). *Journal of Petrology* **48**, 1895–1953. https://doi.org/10.1093/petrology/egm044.

Jicha, B. R. & Kay, S. M. (2018). Quantifying arc migration and the role of forearc subduction erosion in the central Aleutians. *Journal of Volcanology and Geothermal Research* **360**, 84–99. https://doi.org/10.1016/j.jvolgeores.2018.06.016.

Jicha, B. R., Scholl, D. W., Singer, B. S., Yogodzinski, G. M. & Kay, S. M. (2006). Revised age of Aleutian Island arc formation implies high rate of magma production. *Geology* **34**, 661–664. https://doi.org/10.1130/G22433.1.

Johnson, M. C. & Plank, T. (1999). Dehydration and melting experiments constrain the fate of subducted sediments. *Geochemistry, Geophysics, Geosystems* **1**.

Johnston, A. D. & Wyllie, P. J. (1989). The system tonalite–peridotite–H2O at 30 kbar, with applications to hybridization in subduction zone magmatism. *Contributions to Mineralogy and Petrology* **102**, 257–264. https://doi.org/10.1007/BF00373719.

Kay, R. W. (1978). Aleutian magnesian andesites: melts from subducted Pacific Ocean crust. *Journal of Volcanology and Geothermal Research* **4**, 117–132. https://doi.org/10.1016/0377-0273(78)90032-X.

Kay, R. W. (1980). Volcanic arc magmas: implications of a melting-mixing model for element recycling in the crust-upper mantle system. *The Journal of Geology* **88**, 497–522. https://doi.org/10.1086/628541.

Kay, S. M. & Kay, R. W. (1985a). Role of crystal cumulates and the oceanic crust in the formation of the lower crust of the Aleutian arc. *Geology* **13**, 461–464. https://doi.org/10.1130/0091-7613(1985)13<461:ROCCAT>2.0.CO;2.

Kay, S. M. & Kay, R. W. (1985b). Aleutian tholeiitic and calc-alkaline magma series I: the mafic phenocrysts. *Contributions to Mineralogy and Petrology* **90**, 276–290. https://doi.org/10.1007/BF00378268.

Kay, S. M. & Kay, R. W. (1994). Aleutian magmas in space and time. *The Geology of Alaska* **1**, 687–717. https://doi.org/10.1130/DNAG-GNA-G1.687.

Kay, R. W. & Mahlburg Kay, S. (1993). Delamination and delamination magmatism. *Tectonophysics* **219**, 177–189. https://doi.org/10.1016/0040-1951(93)90295-U.

Kay, R. W. & Mahlburg-Kay, S. (1991). Creation and destruction of lower continental crust. *Geologische Rundschau* **80**, 259–278. https://doi.org/10.1007/BF01829365.

Kay, S. M., Kay, R. W. & Citron, G. P. (1982). Tectonic controls on tholeiitic and calc-alkaline magmatism in the Aleutian arc. *Journal of Geophysical Research: Solid Earth* **87**, 4051–4072. https://doi.org/10.1029/JB087iB05p04051.

Kay, S. M., Kay, R. W., Brueckner, H. K. & Rubenstone, J. L. (1983). Tholeiitic Aleutian arc plutonism: the Finger Bay pluton, Adak, Alaska. *Contributions to Mineralogy and Petrology* **82**, 99–116. https://doi.org/10.1007/BF00371179.

Kay, R. W., Rubenstone, J. L. & Kay, S. M. (1986). Aleutian terranes from Nd isotopes. *Nature* **322**, 605–609. https://doi.org/10.1038/322605a0.

Kay, S. M., Kay, R. W., Citron, G. P. & Perfit, M. R. (1990). Calc-alkaline plutonism in the intra-oceanic Aleutian arc, Alaska. *Plutonism from Antarctica to Alaska* **241**, 233–256. https://doi.org/10.1130/SPE241-p233.

Kay, S. M., Godoy, E. & Kurtz, A. (2005). Episodic arc migration, crustal thickening, subduction erosion, and magmatism in the south-Central Andes. *Geological Society of America Bulletin* **117**, 67–88. https://doi.org/10.1130/B25431.1.

Kay, S. M., Jicha, B. R., Citron, G. L., Kay, R. W., Tibbetts, A. K. & Rivera, T. A. (2019). The Calc-Alkaline Hidden Bay and Kagalaska Plutons and the construction of the central Aleutian oceanic arc crust. *Journal of Petrology* **60**, 393–439. https://doi.org/10.1093/petrology/egy119.

van Keken, P. E., Kiefer, B. & Peacock, S. M. (2002). High-resolution models of subduction zones: implications for mineral dehydration reactions and the transport of water into the deep mantle. *Geochemistry, Geophysics, Geosystems* **3**, 1–20. https://doi.org/10.1029/2001GC000256.

Kelemen, P. B., Shimizu, N. & Dunn, T. (1993). Relative depletion of niobium in some arc magmas and the continental crust: partitioning of K, Nb, La and Ce during melt/rock reaction in the upper mantle. *Earth and Planetary Science Letters* **120**, 111–134. https://doi.org/10.1016/0012-821X(93)90234-Z.

Kelemen, P. B., Yogodzinski, G. M. & Scholl, D. W. (2003a). Along-strike variation in the Aleutian Island Arc: genesis of high Mg# andesite and implications for continental crust. *Inside the Subduction Factory* **138**, 223–276. https://doi.org/10.1029/138GM11.

Kelemen, P. B., Hanghøj, K. & Greene, A. R. (2003b). One view of the geochemistry of subduction-related magmatic arcs, with an emphasis on primitive andesite and lower crust. *Treatise on Geochemistry* **3**, 593–659.

Kelley, K. A. & Cottrell, E. (2009). Water and the oxidation state of subduction zone magmas. *American Association for the Advancement of Science* **325**, 605–607. https://doi.org/10.1126/science.1174156.

Kelley, K. A. & Cottrell, E. (2012). The influence of magmatic differentiation on the oxidation state of Fe in a basaltic arc magma. *Earth and Planetary Science Letters* **329-330**, 109–121. https://doi.org/10.1016/j.epsl.2012.02.010.

Kilian, R. & Stern, C. R. (2002). Constraints on the interaction between slab melts and the mantle wedge from adakitic glass in peridotite xenoliths. *European Journal of Mineralogy* **14**, 25–36. https://doi.org/10.1127/0935-1221/02/0014-0025.

Kinzler, R. J. & Grove, T. L. (1992). Primary magmas of mid-ocean ridge basalts 1. Experiments and methods. *Journal of Geophysical Research: Solid Earth* **97**, 6885–6906. https://doi.org/10.1029/91JB02840.

Klemme, S., Blundy, J. D. & Wood, B. J. (2002). Experimental constraints on major and trace element partitioning during partial melting of eclogite. *Geochimica et Cosmochimica Acta* **66**, 3109–3123. https://doi.org/10.1016/S0016-7037(02)00859-1.

Köhler, T. P. & Brey, G. P. (1990). Calcium exchange between olivine and clinopyroxene calibrated as a geothermobarometer for natural peridotites from 2 to 60 kb with applications. *Geochimica et Cosmochimica Acta* **54**, 2375–2388. https://doi.org/10.1016/0016-7037(90)90226-B.

Krawczynski, M. J., Grove, T. L. & Behrens, H. (2012). Amphibole stability in primitive arc magmas: effects of temperature, H2O content, and oxygen fugacity. *Contributions to Mineralogy and Petrology* **164**, 317–339. https://doi.org/10.1007/s00410-012-0740-x.

Leake, B. E., Woolley, A. R., Birch, W. D., Burke, E. A. J., Ferraris, G., Grice, J. D., Hawthorne, F. C., Kisch, H. J., Krivovichev, V. G., Schumacher, J. C., Stephenson, N. C. N. & Whittaker, E. J. (2004). Nomenclature of amphiboles: additions and revisions to the International Mineralogical Association's amphibole nomenclature. *Mineralogical Magazine* **68**, 209–215. https://doi.org/10.1180/0026461046810182.

Li, J., Kornprobst, J., Vielzeuf, D. & Fabriès, J. (1995). An improved experimental calibration of the olivine-spinel geothermometer. *Chinese Journal of Geochemistry* **14**, 68–77. https://doi.org/10.1007/BF02840385.

Luhr, J. F. & Aranda-Gómez, J. J. (1997). Mexican peridotite xenoliths and tectonic terranes: correlations among vent location, texture, temperature, pressure, and oxygen fugacity. *Journal of Petrology* **38**, 1075–1112. https://doi.org/10.1093/petroj/38.8.1075.

Mallik, A., Nelson, J. & Dasgupta, R. (2015). Partial melting of fertile peridotite fluxed by hydrous rhyolitic melt at 2–3 GPa: implications for mantle wedge hybridization by sediment melt and generation of ultrapotassic magmas in convergent margins. *Contributions to Mineralogy and Petrology* **169**, 48. https://doi.org/10.1007/s00410-015-1139-2.

Mallik, A., Dasgupta, R., Tsuno, K. & Nelson, J. (2016). Effects of water, depth and temperature on partial melting of mantle-wedge fluxed by hydrous sediment-melt in subduction zones. *Geochimica et Cosmochimica Acta* **195**, 226–243. https://doi.org/10.1016/j.gca.2016.08.018.

Marsh, B. D. (1976). Some Aleutian andesites: their nature and source. *The Journal of Geology* **84**, 27–45. https://doi.org/10.1086/628172.

Mathez, E. A. (1984). Influence of degassing on oxidation states of basaltic magmas. *Nature* **310**, 371–375. https://doi.org/10.1038/310371a0.

Matsui, Y., Onuma, N., Nagasawa, H., Higuchi, H. & Banno, S. (1977). Crystal structure control in trace element partition between crystal and magma. *Bulletin de Minéralogie* **100**, 315–324.

Mattioli, G. S. & Wood, B. J. (1988). Magnetite activities across the MgAl2O4-Fe3O4 spinel join, with application to thermobarometric estimates of upper mantle oxygen fugacity. *Contributions to Mineralogy and Petrology* **98**, 148–162. https://doi.org/10.1007/BF00402108.

McDonough, W. F. & Sun, S. S. (1995). The composition of the earth. *Chemical Geology* **120**, 223–253. https://doi.org/10.1016/0009-2541(94)00140-4.

Melekhova, E., Blundy, J., Robertson, R. & Humphreys, M. C. (2015). Experimental evidence for polybaric differentiation of primitive arc basalt beneath St. Vincent, Lesser Antilles. *Journal of Petrology* **56**, 161–192. https://doi.org/10.1093/petrology/egu074.

Mukasa, S. B., Blatter, D. L. & Andronikov, A. V. (2007). Mantle peridotite xenoliths in andesite lava at El Peñon, central Mexican Volcanic Belt: isotopic and trace element evidence for melting and metasomatism in the mantle wedge beneath an active arc. *Earth and Planetary Science Letters* **260**, 37–55. https://doi.org/10.1016/j.epsl.2007.05.013.

Münker, C., Wörner, G., Yogodzinski, G. & Churikova, T. (2004). Behaviour of high field strength elements in subduction zones: constraints from Kamchatka–Aleutian arc lavas. *Earth and Planetary Science Letters* **224**, 275–293. https://doi.org/10.1016/j.epsl.2004.05.030.

Nandedkar, R. H., Ulmer, P. & Müntener, O. (2014). Fractional crystallization of primitive, hydrous arc magmas: an experimental study at 0.7 GPa. *Contributions to Mineralogy and Petrology* **167**, 1015. https://doi.org/10.1007/s00410-014-1015-5.

Nicholls, I. A. & Ringwood, A. E. (1973). Effect of water on olivine stability in Tholeiites and the production of silica-saturated magmas in the island-arc environment. *The Journal of Geology* **81**, 285–300. https://doi.org/10.1086/627871.

Nichols, G. T., Wyllie, P. J. & Stern, C. R. (1994). Subduction zone melting of pelagic sediments constrained by melting experiments. *Nature* **371**, 785–788. https://doi.org/10.1038/371785a0.

Parkinson, I. J. & Arculus, R. J. (1999). The redox state of subduction zones: insights from arc-peridotites. *Chemical Geology* **160**, 409–423. https://doi.org/10.1016/S0009-2541(99)00110-2.

Parkinson, I. J. & Pearce, J. A. (1998). Peridotites from the Izu–Bonin–Mariana forearc (ODP leg 125): evidence for mantle melting and melt–mantle interaction in a supra-subduction zone setting. *Journal of Petrology* **39**, 1577–1618. https://doi.org/10.1093/petroj/39.9.1577.

Parkinson, I. J., Arculus, R. J. & Eggins, S. M. (2003). Peridotite xenoliths from Grenada, Lesser Antilles Island arc. *Contributions to Mineralogy and Petrology* **146**, 241–262. https://doi.org/10.1007/s00410-003-0500-z.

Paster, T. P., Schauwecker, D. S. & Haskin, L. A. (1974). The behavior of some trace elements during solidification of the Skaergaard layered series. *Geochimica et Cosmochimica Acta* **38**, 1549–1577. https://doi.org/10.1016/0016-7037(74)90174-4.

Peacock, S. M. (2020). Advances in the thermal and petrologic modeling of subduction zones. *Geosphere* **16**, 936–952. https://doi.org/10.1130/GES02213.1.

Peacock, S. M., Rushmer, T. & Thompson, A. B. (1994). Partial melting of subducting oceanic crust. *Earth and Planetary Science Letters* **121**, 227–244. https://doi.org/10.1016/0012-821X(94)90042-6.

Peacock, S. M., van Keken, P. E., Holloway, S. D., Hacker, B. R., Abers, G. A. & Fergason, R. L. (2005). Thermal structure of the Costa Rica–Nicaragua subduction zone. *Physics of the Earth and Planetary Interiors* **149**, 187–200. https://doi.org/10.1016/j.pepi.2004.08.030.

Peltonen, P. (1995). Crystallization and re-equilibration of zoned chromite in ultramafic cumulates, Vammala Ni-belt, southwestern Finland. *The Canadian Mineralogist* **33**, 521–535.

Perfit, M. R., Gust, D. A., Bence, A. E., Arculus, R. J. & Taylor, S. R. (1980). Chemical characteristics of island-arc basalts: implications for mantle sources. *Chemical Geology* **30**, 227–256. https://doi.org/10.1016/0009-2541(80)90107-2.

Pichavant, M. & Macdonald, R. (2007). Crystallization of primitive basaltic magmas at crustal pressures and genesis of the calc-alkaline igneous suite: experimental evidence from St Vincent,

Lesser Antilles arc. *Contributions to Mineralogy and Petrology* **154**, 535–558. https://doi.org/10.1007/s00410-007-0208-6.

Poli, S. & Schmidt, M. W. (2002). Petrology of subducted slabs. *Annual Review of Earth and Planetary Sciences* **30**, 207–235. https://doi.org/10.1146/annurev.earth.30.091201.140550.

Putirka, K. (2016). Amphibole thermometers and barometers for igneous systems and some implications for eruption mechanisms of felsic magmas at arc volcanoes. *American Mineralogist* **101**, 841–858. https://doi.org/10.2138/am-2016-5506.

Rapp, R. P. & Watson, E. B. (1995). Dehydration melting of Metabasalt at 8-32 kbar: implications for continental growth and crust-mantle recycling. *Journal of Petrology* **36**, 891–931. https://doi.org/10.1093/petrology/36.4.891.

Rapp, R. P., Watson, E. B. & Miller, C. F. (1991). Partial melting of amphibolite/eclogite and the origin of Archean trondhjemites and tonalites. *Precambrian Research* **51**, 1–25. https://doi.org/10.1016/0301-9268(91)90092-O.

Rapp, R. P., Shimizu, N., Norman, M. D. & Applegate, G. S. (1999). Reaction between slab-derived melts and peridotite in the mantle wedge: experimental constraints at 3.8 GPa. *Chemical Geology* **160**, 335–356. https://doi.org/10.1016/S0009-2541(99)00106-0.

Richards, J. P. (2015). The oxidation state, and sulfur and cu contents of arc magmas: implications for metallogeny. *Lithos* **233**, 27–45. https://doi.org/10.1016/j.lithos.2014.12.011.

Ridolfi, F. (2021). Amp-TB2: an updated model for calcic amphibole thermobarometry. *Minerals* **11**, 324. https://doi.org/10.3390/min11030324.

Ringwood, A. E. (1990). Slab-mantle interactions: 3. Petrogenesis of intraplate magmas and structure of the upper mantle. *Chemical Geology* **82**, 187–207. https://doi.org/10.1016/0009-2541(90)90081-H.

Ringwood, A. E. & Green, D. H. (1966). An experimental investigation of the gabbro-eclogite transformation and some geophysical implications. *Tectonophysics* **3**, 383–427. https://doi.org/10.1016/0040-1951(66)90009-6.

Rubatto, D. & Hermann, J. (2003). Zircon formation during fluid circulation in eclogites (Monviso, Western Alps): implications for Zr and Hf budget in subduction zones. *Geochimica et Cosmochimica Acta* **67**, 2173–2187. https://doi.org/10.1016/S0016-7037(02)01321-2.

Rudnick, R. L. (1995). Making continental crust. *Nature* **378**, 571–578. https://doi.org/10.1038/378571a0.

Rudnick, R. L. & Gao, S. (2003). Composition of the continental crust. *Treatise on Geochemistry* **3**, 1–64. https://doi.org/10.1016/B0-08-043751-6/03016-4.

Salters, V. J. & Stracke, A. (2004). Composition of the depleted mantle. *Geochemistry, Geophysics, Geosystems* **5**. https://doi.org/10.1029/2003GC000597.

Schiano, P., Monzier, M., Eissen, J.-P., Martin, H. & Koga, K. T. (2010). Simple mixing as the major control of the evolution of volcanic suites in the Ecuadorian Andes. *Contributions to Mineralogy and Petrology* **160**, 297–312. https://doi.org/10.1007/s00410-009-0478-2.

Schmidt, M. W. & Jagoutz, O. (2017). The global systematics of primitive arc melts. *Geochemistry, Geophysics, Geosystems* **18**, 2817–2854. https://doi.org/10.1002/2016GC006699.

Schmidt, M. W. & Poli, S. (1998). Experimentally based water budgets for dehydrating slabs and consequences for arc magma generation. *Earth and Planetary Science Letters* **163**, 361–379. https://doi.org/10.1016/S0012-821X(98)00142-3.

Sekine, T. & Wyllie, P. J. (1982). The system granite–peridotite–H2O at 30 kbar, with applications to hybridization in subduction zone magmatism. *Contributions to Mineralogy and Petrology* **81**, 190–202. https://doi.org/10.1007/BF00371296.

Sen, C. & Dunn, T. (1994). Dehydration melting of a basaltic composition amphibolite at 1.5 and 2.0 GPa: implications for the origin of adakites. *Contributions to Mineralogy and Petrology* **117**, 394–409. https://doi.org/10.1007/BF00307273.

Sen, C. & Dunn, T. (1995). Experimental modal metasomatism of a spinel lherzolite and the production of amphibole-bearing peridotite. *Contributions to Mineralogy and Petrology* **119**, 422–432. https://doi.org/10.1007/BF00286939.

Shaw, D. M. (2000). Continuous (dynamic) melting theory revisited. *The Canadian Mineralogist* **38**, 1041–1063. https://doi.org/10.2113/gscanmin.38.5.1041.

Shaw, D. M. (2006) *Trace Elements in Magmas: A Theoretical Treatment*. Cambridge University Press.

Shejwalkar, A. & Coogan, L. A. (2013). Experimental calibration of the roles of temperature and composition in the ca-in-olivine geothermometer at 0.1MPa. *Lithos* **177**, 54–60. https://doi.org/10.1016/j.lithos.2013.06.013.

Siegrist, M., Yogodzinski, G., Bizimis, M., Fournelle, J., Churikova, T., Dektor, C. & Mobley, R. (2019). Fragments of Metasomatized Fore-arc: origin and implications of mafic and ultramafic xenoliths from Kharchinsky Volcano, Kamchatka. *Geochemistry, Geophysics, Geosystems* **20**, 4426–4456. https://doi.org/10.1029/2019GC008478.

Sisson, T. W. & Grove, T. L. (1993). Experimental investigations of the role of H 2 O in calc-alkaline differentiation and subduction zone magmatism. *Contributions to Mineralogy and Petrology* **113**, 143–166. https://doi.org/10.1007/BF00283225.

Sisson, T. W. & Kelemen, P. B. (2018). Near-solidus melts of MORB + 4 wt% H2O at 0.8–2.8 GPa applied to issues of subduction magmatism and continent formation. *Contributions to Mineralogy and Petrology* **173**, 70. https://doi.org/10.1007/s00410-018-1494-x.

Skora, S. & Blundy, J. (2010). High-pressure hydrous phase relations of radiolarian clay and implications for the involvement of subducted sediment in arc magmatism. *Journal of Petrology* **51**, 2211–2243. https://doi.org/10.1093/petrology/egq054.

Sparks, R. S. J. & Marshall, L. A. (1986). Thermal and mechanical constraints on mixing between mafic and silicic magmas. *Journal of Volcanology and Geothermal Research* **29**, 99–124. https://doi.org/10.1016/0377-0273(86)90041-7.

Stamper, C. C., Blundy, J. D., Arculus, R. J. & Melekhova, E. (2014a). Petrology of plutonic xenoliths and volcanic rocks from Grenada, Lesser Antilles. *Journal of Petrology* **55**, 1353–1387. https://doi.org/10.1093/petrology/egu027.

Stamper, C. C., Melekhova, E., Blundy, J. D., Arculus, R. J., Humphreys, M. C. S. & Brooker, R. A. (2014b). Oxidised phase relations of a primitive basalt from Grenada, Lesser Antilles. *Contributions to Mineralogy and Petrology* **167**, 954. https://doi.org/10.1007/s00410-013-0954-6.

Stern, C. R. (1991). Role of subduction erosion in the generation of Andean magmas. *Geology* **19**, 78. https://doi.org/10.1130/0091-7613(1991)019<0078:ROSEIT>2.3.CO;2.

Streck, M. J., Leeman, W. P. & Chesley, J. (2007). High-magnesian andesite from Mount Shasta: a product of magma mixing and contamination, not a primitive mantle melt. *Geology* **35**, 351. https://doi.org/10.1130/G23286A.1.

Sun, S. S. (1980). Lead isotopic study of young volcanic rocks from mid-ocean ridges, ocean islands and island arcs. Philosophical transactions of the Royal Society of London. *Series A, Mathematical and Physical Sciences* **297**, 409–445.

Syracuse, E. M., van Keken, P. E. & Abers, G. A. (2010). The global range of subduction zone thermal models. *Physics of the*

Earth and Planetary Interiors **183**, 73–90. https://doi.org/10.1016/j.pepi.2010.02.004.

Tamura, A. & Arai, S. (2006). Harzburgite–dunite–orthopyroxenite suite as a record of supra-subduction zone setting for the Oman ophiolite mantle. *Lithos* **90**, 43–56. https://doi.org/10.1016/j.lithos.2005.12.012.

Turner, S. J. & Langmuir, C. H. (2022a). Sediment and ocean crust both melt at subduction zones. *Earth and Planetary Science Letters* **584**, 117424. https://doi.org/10.1016/j.epsl.2022.117424.

Turner, S. J. & Langmuir, C. H. (2022b). A quantitative framework for global variations in arc geochemistry. *Earth and Planetary Science Letters* **584**, 117411. https://doi.org/10.1016/j.epsl.2022.117411.

Ulmer, P., Kaegi, R. & Müntener, O. (2018). Experimentally derived intermediate to silica-rich arc magmas by fractional and equilibrium crystallization at 1·0 GPa: an evaluation of phase relationships, compositions, liquid lines of descent and oxygen fugacity. *Journal of Petrology* **59**, 11–58. https://doi.org/10.1093/petrology/egy017.

Vannucci, R., Tiepolo, M., Defant, M. J. & Kepezhinskas, P. (2007). The metasomatic record in the shallow peridotite mantle beneath Grenada (Lesser Antilles arc). *Lithos* **99**, 25–44. https://doi.org/10.1016/j.lithos.2007.05.007.

Vigneresse, J. L., Barbey, P. & Cuney, M. (1996). Rheological transitions during partial melting and crystallization with application to felsic magma segregation and transfer. *Journal of Petrology* **37**, 1579–1600. https://doi.org/10.1093/petrology/37.6.1579.

Wada, I. & Wang, K. (2009). Common depth of slab-mantle decoupling: reconciling diversity and uniformity of subduction zones. *Geochemistry, Geophysics, Geosystems* **10**. https://doi.org/10.1029/2009GC002570.

Wood, B. J. & Virgo, D. (1989). Upper mantle oxidation state: ferric iron contents of lherzolite spinels by 57Fe Mössbauer spectroscopy and resultant oxygen fugacities. *Geochimica et Cosmochimica Acta* **53**, 1277–1291. https://doi.org/10.1016/0016-7037(89)90062-8.

Wood, B. J., Bryndzia, L. T. & Johnson, K. E. (1990). Mantle oxidation state and its relationship to tectonic environment and fluid speciation. *Science* **248**, 337–345. https://doi.org/10.1126/science.248.4953.337.

Yasuda, A., Fujii, T. & Kurita, K. (1994). Melting phase relations of an anhydrous mid-ocean ridge basalt from 3 to 20 GPa: implications for the behavior of subducted oceanic crust in the mantle. *Journal of Geophysical Research: Solid Earth* **99**, 9401–9414. https://doi.org/10.1029/93JB03205.

Yogodzinski, G. M. & Kelemen, P. B. (1998). Slab melting in the Aleutians: implications of an ion probe study of clinopyroxene in primitive adakite and basalt. *Earth and Planetary Science Letters* **158**, 53–65. https://doi.org/10.1016/S0012-821X(98)00041-7.

Yogodzinski, G. M. & Kelemen, P. B. (2007). Trace elements in clinopyroxenes from Aleutian xenoliths: implications for primitive subduction magmatism in an island arc. *Earth and Planetary Science Letters* **256**, 617–632. https://doi.org/10.1016/j.epsl.2007.02.015.

Yogodzinski, G. M., Volynets, O. N., Koloskov, A. V., Seliverstov, N. I. & Matvenkov, V. V. (1994). Magnesian Andesites and the subduction component in a strongly calc-alkaline series at Piip Volcano, far Western Aleutians. *Journal of Petrology* **35**, 163–204. https://doi.org/10.1093/petrology/35.1.163.

Yogodzinski, G. M., Brown, S. T., Kelemen, P. B., Vervoort, J. D., Portnyagin, M., Sims, K. W. & Werner, R. (2015). The role of subducted basalt in the source of island arc magmas: evidence from seafloor lavas of the western Aleutians. *Journal of Petrology* **56**, 441–492. https://doi.org/10.1093/petrology/egv006.

Yogodzinski, G. M., Kelemen, P. B., Hoernle, K., Brown, S. T., Bindeman, I., Vervoort, J. D. & Werner, R. (2017). Sr and O isotopes in western Aleutian seafloor lavas: implications for the source of fluids and trace element character of arc volcanic rocks. *Earth and Planetary Science Letters* **475**, 169–180. https://doi.org/10.1016/j.epsl.2017.07.007.